Resonance modulation, annihilation and generation of antiresonance and antiphasonance in 3D neuronal systems: interplay of resonant and amplifying currents with slow dynamics

Horacio G. Rotstein[1]

[1] Department of Mathematical Sciences
New Jersey Institute of Technology
Newark, NJ 07102, USA

December 2, 2016

Abstract

Subthreshold (membrane potential) resonance and phasonance (preferred amplitude and zero-phase responses to oscillatory inputs) in single neurons arise from the interaction between positive and negative feedback effects provided by relatively fast amplifying currents and slower resonant currents. In 2D neuronal systems, amplifying currents are required to be slaved to voltage (instantaneously fast) for these phenomena to occur. In higher dimensional systems, additional currents operating at various effective time scales may modulate and annihilate existing resonances and generate antiresonance (minimum amplitude response) and antiphasonance (zero-phase response with phase monotonic properties opposite to phasonance). We use mathematical modeling, numerical simulations and dynamical systems tools to investigate the mechanisms underlying these phenomena in 3D linear models, which are obtained as the linearization of biophysical (conductance-based) models. We characterize the parameter regimes for which the system exhibits the various types of behavior mentioned above in the rather general case in which the underlying 2D system exhibits resonance. We consider two cases: (i) the interplay of two resonant gating variables, and (ii) the interplay of one resonant and one amplifying gating variables. Increasing levels of an amplifying current cause (i) a response amplification if the amplifying current is faster than the resonant current, (ii) resonance and phasonance attenuation and annihilation if the amplifying and resonant currents have identical dynamics, and (iii) antiresonance and antiphasonance if the amplifying current is slower than the resonant current. We investigate the underlying mechanisms by extending the envelope-plane diagram approach developed in previous work (for 2D systems) to three dimensions to include the additional gating variable, and constructing the corresponding envelope curves in these envelope-space diagrams. We find that antiresonance and antiphasonance emerge as the result of an asymptotic boundary layer problem in the frequency domain created by the different balances between the intrinsic time constants of the cell and the input

1

frequency f as it changes. For large enough values of f the envelope curves are quasi-2D and the impedance profile decrease with the input frequency. In contrast, for $f \ll 1$ the dynamics is quasi-1D and the impedance profile increases above the limiting value in the other regime. Antiresonance is created because the continuity of the solution requires the impedance profile to connect the portions belonging to the two regimes. If in doing so the phase profile crosses the zero value, then antiphasonance is also generated.

1 Introduction

The response of a neuron to oscillatory inputs can be characterized by the so-called impedance (Z) and phase (ϕ) profiles, which are the curves of the impedance amplitude (or simply impedance) and phase-shift (or simply phase) as a function of the input frequency (f) respectively [1–3]. A neuron exhibits subthreshold (membrane potential) resonance and phasonance if the impedance profile peaks at a nonzero input (resonant) frequency f_{res} and the phase profile vanishes at a non-zero input (phasonant) frequency f_{phas}. The latter indicates that the input and output peak at the same time for $f = f_{phas}$. Several neuron types have been shown to exhibit subthreshold resonance and phasonance in response to oscillatory inputs in both current and voltage clamp experiments and in models [1, 2, 4–40]. Subthreshold resonance, phasonance and intrinsic oscillations are related, but different phenomena, and neurons may exhibit one(s) in the absence of the other(s) [2–4, 41, 42].

The functionality of neuronal resonance has not been fully established yet. However, several lines of work have demonstrated the role of resonance for network oscillatory activity either directly or indirectly [38, 43–47] both experimentally and theoretically. The role played by resonance in network oscillations is further supported by the fact that the resonant frequency of certain neuron types coincides with the oscillatory frequency of the networks in which they are embedded [12, 13, 26, 48]

Subthreshold resonance results from the interaction between positive and negative feedback effects provided by the amplifying and resonant gating variables that govern the dynamics of the participating ionic currents. Neurons with only a passive leak current are low-pass filters: the impedance profile is a decreasing function of f and the response is always delayed. Resonance requires the presence of a gating variable that opposes changes in voltage such as these associated to the so-called resonant currents (e.g., hyperpolarization-activated mixed-cation I_h and slow-potassium I_{Ks}). The gating variables associated to so-called amplifying currents (e.g., persistent sodium I_{Nap} and inward-rectifying potassium I_{Kir}) favor changes in voltage and therefore enhance the voltage response in the resonant frequency band [1–3].

In previous work we have carried out a thorough analysis of subthreshold resonance and phasonance in 2D linearized and nonlinear neuronal models of quadratic type having a fast (instantaneous) amplifying current and a slower resonant current [3, 41, 42]. By combining bio-physical (conductance-based) modeling, numerical simulations and dynamical systems tools we have identified the biophysical and dynamic mechanisms underlying the generation of reso-nance and phasonance and described the effects that changes in the maximal conductances and other model parameters have on f_{res}, f_{phas} and the additional attributes characterizing the shapes of the impedance and phase profiles. In these studies we have used linear and quadratic models, representing the linearization and "quadratization", respectively, of biophysical mod-els of Hodgkin-Huxley type [49] describing the neuronal subthreshold dynamics, and we have investigated the role played by various types of resonant and amplifying currents, and their

combinations, through these simplified models.

For 2D models to exhibit resonance the fast amplifying gating variable is constrained to be instantaneously fast and slaved to voltage. These models fail to capture complex phenomena such as the presence of troughs in the impedance profile that have been experimentally observed in hippocampal interneurons [18] and more recently in the so-called LP neurons of the crab stomatogastric ganglion pyloric network [37], and have been shown theoretically to emerge in models with slower amplifying gating variables [2]. We refer to this phenomenon as antiresonance and the associated emergence of an additional zero in the phase profile as antiphasonance, and we refer to the corresponding characteristic frequencies as f_{ares} and f_{aphas}, respectively. For antiresonance and antiphasonance to occur the additional degree of freedom provided by the slower amplifying gating variable is necessary. To our knowledge, the mechanisms of generation of antiresonance and antiphasonance as well as the mechanisms that govern the modulation of underlying 2D resonances by the interaction between two ionic currents with slow dynamics and either the similar or opposite feedback effects in oscillatory forced systems have not been investigated.

The goal of this paper is to address these issues for 3D linear models representing the linearization of conductance-based models. These models have a resonant gating variable and an additional gating variable that can be either resonant or amplifying. This gives rise to two types of interactions between cooperative and competitive feedback effects operating at comparable or different time scales. Antiresonance and antiphasonance occur when the amplifying gating variable is slower than the resonant one. The antiresonant patterns, in the presence of an underlying 2D resonance, are shaped by a trade-off between the time constant and linearized conductance of this amplifying gating variable. In [50] we have investigated how these different ways of interaction shape the intrinsic subthreshold oscillatory properties of linearized and nonlinear models and the complex dependence of these oscillatory patterns on the model parameters. Here we extend our study to models receiving oscillatory forcing. As for 2D systems, this extension is not straightforward, primarily because even linear systems can exhibit subthreshold resonance in the absence of intrinsic subthreshold oscillations [2,3,41,42].

For our mechanistic analysis we extend the envelope-plane diagram approach developed in [41] (see also [42]) to the 3D space to include the additional gating variable. We view the dynamics of the oscillatory forced 3D system as the result of the response limit cycle trajectories tracking the oscillatory motion of the voltage nullsurface as time progresses. This allows us to construct the so-called envelope curves in the 3D envelope-space diagram. The envelope curves consist of the points corresponding to the peaks of these response limit cycle trajectories in the v-direction (maximum voltage and the corresponding values of the other coordinates). The envelope-space diagrams contain geometric and dynamic information about the frequency response properties of the system to oscillatory inputs, and are the frequency analogous to the phase-space diagrams. The envelope curves are trajectories in the envelope-space diagrams parametrized by the input frequency as trajectories in the phase-space diagrams are curves parametrized by time. This approach allow us to identify the principles that govern (i) the modulation and annihilation of existing resonances, and (ii) the generation of antiresonance and antiphasonance. In addition, it allows us to determine the conditions under which these phenomena occur. For visualization purposes, we use projections of the envelope-space diagrams onto the relevant planes for the participating variables in addition to the 3D diagrams.

An important outcome of this analysis is the identification of the mechanism of generation of antiresonance and antiphasonance as an asymptotic boundary layer problem in the frequency

domain. This is the result of the different balances between the input frequency f and the cell's intrinsic time constants (independent of f) as f changes. For values of f away from zero the dynamics are 2D and governed by the underlying 2D resonant system independently of the slow amplifying variable. In contrast, for values of f close to zero the dynamics are quasi-1D and the resistance $Z(0)$, which depends on the maximal conductance of the slow variable, increases above the limit of the impedance for the 2D system as f approaches zero. The trough in the impedance profile is created because the continuity of the solution requires the impedance profile to connect the portions belonging to the two regimes. If in doing so the phase profile crosses the zero value, then antiphasonance is also generated.

The investigation of the voltage response to sinusoidal inputs has typically focused on how preferred frequency responses are generated by the presence of a negative feedback (resonance and phasonance) and how the voltage response is enhanced at the preferred frequency band by the presence of a positive feedback (amplification). While these two processes are often discussed separately [1,2], they are intertwined: amplifying currents cannot generate resonance in the absence of a resonant current, but they can modify the values the resonant and phasonant frequencies as well as other attributes of the impedance and phase profiles [3,41,51]. Therefore, the study presented here includes the mechanisms of selection of the resonant and phasonant frequencies in addition to the generation and amplification of resonance.

The outline of the paper is as follows. In Section 3.1 we revisit the biophysical and dynamic mechanisms of generation of resonance and phasonance in 2D models (voltage v and a resonant gating variable x_1). For future use, we introduce the description of so-called dynamic phase-plane for 2D oscillatory forced systems, which include the envelope-plane diagrams and envelope-curves mentioned above. In Section 3.2 we discuss the three limiting and special cases where the voltage response dynamics of the 3D system (v, x_1 and a second gating variable x_2) reduces to the voltage response dynamics for quasi-2D systems, and therefore they can be understood in terms of the results from previous work. In Section 3.3 we identify the basic mechanisms of modulation and annihilation of resonance / phasonance and the generation of antiresonance / antiphasonance in the forced 3D model. As a baseline case for our study we use a representative set of parameter values for the underlying 2D system such that this 2D system exhibits resonance but no intrinsic oscillations. In Section 3.4 we extend this investigation to understand how the trade-off between the maximal conductance and time constant of the x_2 shape the preferred response properties of the 3D model identified in Section 3.3 using the same baseline parameter values as we used there . We consider the interplay of both (i) two resonant gating variables, and (ii) one resonant and one amplifying gating variables. In Section 3.5 we investigate the dynamic mechanisms of resonance modulation and annihilation and the generation of antiresonance and antiphasonance. To this end, we extend the dynamic phase-space approach discussed in Section 3.1 to include the three variables (voltage and the two gating variables). The mechanistic principles we extract from this study have a more general validity than the specific sets of parameter values considered in the previous sections. Finally, in Section 4 we discuss our results, limitations and implications for neuronal dynamics.

4

2   Methods

2.1   Conductance-based models

We use the following biophysical (conductance-based) models of Hodgkin-Huxley type [49,52] to describe the neuronal subthreshold dynamics

$$C\frac{dV}{dt} = -I_L - \sum_j I_j + I_{app} + I_{in}(t), \tag{1}$$

$$\frac{dx_j}{dt} = \frac{x_{j,\infty}(V) - x_j}{\tau_{k,j}(V)}, \qquad j = 1, 2. \tag{2}$$

In the current-balance equation (1), V is the membrane potential (mV), t is time (ms), C is the membrane capacitance (μF/cm^2), I_{app} is the applied bias (DC) current (μA/cm^2), $I_L = G_L(V - E_L)$ is the leak current, and $I_j = G_j x_j, (V - E_j)$ are generic expressions for ionic currents (with j an index) with maximal conductance G_j (mS/cm^2) and reversal potentials E_j (mV) respectively. The dynamics of the gating variables x_j are governed by the kinetic equations (2) where $x_{j,\infty}(V)$ and $\tau_{j,x}(V)$ are the voltage-dependent activation/inactivation curves and time constants respectively. The generic ionic currents I_j we consider here are restricted to have a single gating variable x_j and to be linear in x_j. This is typically the case for persistent sodium (I_{Nap}), h- (hyperpolarization-activated, mixed-cation, inward), and slow-potassium (M-type) (I_{Ks}) currents. Our discussion and results can be easily adapted to include ionic currents having two gating variables raised to powers different from one such as T-type calcium and A-type potassium currents [1].

The input current $I_{in}(t)$ (μA/cm^2) in eq. (1) has the form

$$I_{in}(t) = A_{in}\,sin(\Omega\,t) \qquad \text{with} \qquad \Omega = \frac{2\pi f}{T}, \tag{3}$$

where $T = 1000$ ms and f is the input frequency (Hz).

In this paper we focus on 3D models describing the dynamics of V and the two gating variables. Additional currents whose gating variables evolve on a very fast time scale (as compared to the other variables) can be included by using the adiabatic approximation $x_k = x_{k,\infty}(V)$. Here we include one such fast current $I_3 = G_3\,x_{3,\infty}(V)\,(V - E_3)$. Additional fast currents can be included without significantly changing the formalism used here.

2.2   Linearized conductance-based models

Linearization of the autonomous part ($I_{in}(t) = 0$) of system (1)-(2) around the fixed-point $(\bar{V}, \bar{x}_1, \bar{x}_2)$ yields [2]

$$C\frac{dv}{dt} = -g_L v - g_1 w_1 - g_2 w_2 + I_{in}(t), \tag{4}$$

$$\bar{\tau}_1\frac{dw_1}{dt} = v - w_1, \tag{5}$$

$$\bar{\tau}_2\frac{dw_2}{dt} = v - w_2, \tag{6}$$

5

where

$$v = V - \bar{V}, \qquad w_1 = \frac{x_1 - \bar{x}_1}{x'_{1,\infty}(\bar{V})}, \qquad w_2 = \frac{x_2 - \bar{x}_2}{x'_{2,\infty}(\bar{V})}, \tag{7}$$

$$\bar{x}_j = x_{j,\infty}(\bar{V}), \qquad \bar{\tau}_j = \tau_{x,j}(\bar{V}) \qquad j = 1, 2, \tag{8}$$

$$g_j = G_j \, x'_{j,\infty}(\bar{V}) \, (\bar{V} - E_j), \qquad j = 1, 2, 3, \tag{9}$$

and

$$g_L = G_L + G_1 \, x_{1,\infty}(\bar{V}) + G_2 \, x_{2,\infty}(\bar{V}) + G_3 \, x_{3,\infty}(\bar{V}) + g_3. \tag{10}$$

Note that the gating variables w_1 and w_2 in (7) have units of voltage ($[v] = [w_1] = $V).

The effective leak conductance g_L (10) contains information about the biophysical leak conductance G_L, the ionic conductances, and their associated voltage-dependent activation / inactivation curves. The fast ionic current I_3 contributes to g_L with an additional term g_3. The signs of the effective ionic conductances g_j determine whether the associated gating variables are either resonant ($g_j > 0$) or amplifying ($g_j < 0$) [1, 2]. Specific examples are the gating variables associated to I_h (resonant), I_{Ks} (resonant), I_{Nap} (amplifying) and I_{Kir} (amplifying). All terms in g_L are positive except for the last one that can be either positive or negative. Specifically, g_L can become negative for negative enough values of g_3. This and the other linearized conductances are affected not only by the respective biophysical conductances, but also by the magnitudes and signs of the activation ($\sigma < 0$) and inactivation ($\sigma > 0$) curves and their derivatives, which are typically given by expressions of the form

$$x_\infty(V) = \left(1 + e^{\sigma \frac{V - V_{1/2}}{V_{slp}}} \right)^{-1} \tag{11}$$

and

$$x'_\infty(V) = -\frac{\sigma}{V_{slp}} \left(1 + e^{\sigma \frac{V - V_{1/2}}{V_{slp}}} \right)^{-2} e^{\sigma \frac{V - V_{1/2}}{V_{slp}}} \tag{12}$$

where $V_{1/2}$ and $V_{slp} > 0$ are constants.

2.3   Biophysical- and geometric-based rescaled models

System (4)-(6) can be rescaled in order to reduce the number of parameters of the autonomous part (from six to four) and to capture the relative effects of the linearized conductances g_1 and g_2 and their time constants $\bar{\tau}_1$ and $\bar{\tau}_2$. Here we use two different rescalings. The so-called biophysical rescaling uses dimensionless conductances and is appropriate for the analysis of the dependence of the resonant properties in terms of the ionic conductances and the role of the time constants in effectively strengthening these conductances. It is close to the one that combines the biophysical description with the time-scale separation between variables and has been used in [2] (see also [3]). The so-called geometric rescaling is amenable for the mechanistic analysis using dynamical systems tools ("dynamic" phase-space analysis) and is an extension of the one we used in [41]. For the biophysically related questions we will use the original linearized (4)-(6) model. However, the biophysical rescaling shows that the principles extracted from our study are valid beyond the representative parameter values we used.

2.3.1 Rescaled model I: Biophysical dimensionless conductances

Define the following dimensionless time

$$\hat{t} = \frac{t}{\bar{\tau}_1} \tag{13}$$

and parameters

$$\gamma_l = \frac{g_l \bar{\tau}_1}{C} \qquad \gamma_1 = \frac{g_1 \bar{\tau}_1}{C} \qquad \gamma_2 = \frac{g_2 \bar{\tau}_1}{C} \qquad \eta = \frac{\bar{\tau}_1}{\bar{\tau}_2} \tag{14}$$

Substitutying into (4)-(5) we obtain

$$\frac{dv}{d\hat{t}} = -\gamma_l v - \gamma_1 w_1 - \gamma_2 w_2 + \hat{I}_{in}(\hat{t}) \tag{15}$$

$$\frac{dw_1}{d\hat{t}} = v - w_1 \tag{16}$$

$$\frac{dw_2}{d\hat{t}} = \eta \left[v - w_2 \right] \tag{17}$$

where

$$\hat{I}_{in}(t) = \hat{A}_{in} \, sin(2\pi f \hat{t}/\hat{T}) \qquad \text{with} \qquad \hat{A}_{in} = \frac{A_{in} \bar{\tau}_1}{C} \tag{18}$$

with $\hat{T} = T/\bar{\tau}_1 = 1000/\tau_1$. Note that $[f] = $ Hz, and $[v] = [w_1] = [w_2] = $ V.

2.3.2 Rescaled model II: Geometric/dynamic description

Define the following dimensionless time and (dimensional) voltage variables

$$\hat{t} = \frac{g_l}{C} t \qquad \hat{v} = \frac{g_l}{g_1} v \tag{19}$$

and parameters

$$\alpha = \frac{g_1}{g_l} \qquad \epsilon = \frac{C}{\bar{\tau}_1 g_l} \qquad \kappa = \frac{g_2}{g_1} \qquad \eta = \frac{\bar{\tau}_1}{\bar{\tau}_2}. \tag{20}$$

Substitutying into (4)-(5) we obtain

$$\frac{dv}{d\hat{t}} = -v - w_1 - \kappa \, w_2 + \hat{I}_{in}(\hat{t}), \tag{21}$$

$$\frac{dw_1}{d\hat{t}} = \epsilon \left[\alpha v - w_1 \right], \tag{22}$$

$$\frac{dw_2}{d\hat{t}} = \epsilon \, \eta \left[\alpha v - w_2 \right] \tag{23}$$

where

$$\hat{I}_{in}(t) = \hat{A}_{in} \, sin(2\pi f \hat{t}/\hat{T}) \qquad \text{with} \qquad \hat{A}_{in} = \frac{A_{in}}{g_1}, \tag{24}$$

7

with $\hat{T} = Tg_l/C = 1000g_l/C$. Note that $[f] = $ Hz, and $[v] = [w_1] = [w_2] = $ V.

System (21)-(23) can be thought of as a 3D extension of the 2D linear system investigated in [41] to which it reduces for $\kappa = 0$. Geometrically, the parameter α is the slope of the w-nullcline and can be thought of as representing the strength of the gain of the feedback in the linearized system. The parameter ϵ represents the time scale separation between v and w_1 and η represents the time scale separation between w_1 and w_2.

Since for resonant gating variables $g_1 > 0$, the sign of both α and ϵ depends on whether g_L is positive or negative. In the absence of fast amplifying currents ($G_3 = g_3 = 0$), $g_L > 0$ and then both $\alpha > 0$ and $\epsilon > 0$. When an amplifying current is present and its contribution to g_L is small enough, the sign of both α and ϵ remains positive. However, when stronger contributions of the fast amplifying current causes g_L to be negative, the sign of both α and ϵ are also negative. Since resonance becomes amplified as g_L decreases [3], we expect resonance to be more amplified for negative values of both ϵ and α as compared to positive ones as in [41]. The cases including values of α and ϵ having different signs are excluded from this study since the underlying autonomous system is either unstable (saddle) or stable (node) but does not exhibit resonance [41].

2.3.3   Linking the rescalings I and II

The parameters in the autonomous parts of the rescaled systems (15)-(17) and (21)-(23) are related by the following equations

$$\epsilon = \frac{1}{\gamma_l}, \qquad \alpha = \frac{\gamma_1}{\gamma_l}, \qquad \kappa = \frac{\gamma_2}{\gamma_1}. \tag{25}$$

The dimensionless parameter η is common to both rescaled models.

2.4   Decoupling the input frequency from the oscillatory input

For the type of analysis we present in this paper it is useful to rescale time $t \to t/f$ in order to separate the effect of the input frequency f from the input's time dependence [42]. After dropping the "hat" from the time and input current, system (4)-(6) becomes

$$\frac{dv}{dt} = \frac{g_L}{Cf}\left[-v - \frac{g_1}{g_L}w_1 - \frac{g_2}{g_L}w_2 + \frac{I_{in,1}}{g_L}(t)\right], \tag{26}$$

$$\frac{dw_1}{dt} = \frac{1}{\bar{\tau}_1 f}\left[v - w_1\right], \tag{27}$$

$$\frac{dw_2}{dt} = \frac{1}{\bar{\tau}_2 f}\left[v - w_2\right], \tag{28}$$

where

$$I_{in,1}(t) = A_{in}sin(2\pi t/1000). \tag{29}$$

In system (26)-(28) the sinusoidal input function has the same frequency for all values of f, which affects the speed of the voltage response. Similarly, system (21)-(23) becomes

$$\frac{dv}{dt} = \frac{1}{f}\left[-v - w_1 - \kappa w_2 + I_{in,1}(t)\right], \tag{30}$$

8

$$\frac{dw_1}{dt} = \frac{\epsilon}{f} \left[\alpha v - w_1 \right], \tag{31}$$

$$\frac{dw_2}{dt} = \frac{\epsilon \, \eta}{f} \left[\alpha v - w_2 \right]. \tag{32}$$

In geometric / dynamic terms, this shows that the input frequency f affects the speed of the trajectories in the phase space without affecting the direction of the underlying vector field [41, 42]. Additionally, this transformation highlights the different balances that arise between the effective time constant (f^{-1}) "imposed" by the oscillatory input and the cell's intrinsic time constants as the input frequency changes.

When w_1 and w_2 are identical (and have the same initial conditions) the 3D system (30)-(32) is effectively 2D. By substituting these variables by w eqs. (30)-(32) reduce to

$$\frac{dv}{dt} = \frac{1}{f} \left[-v - (1 + \kappa) \, w + I_{in,1}(t) \right], \tag{33}$$

$$\frac{dw}{dt} = \frac{\epsilon}{f} \left[\alpha v - w \right], \tag{34}$$

In what follows we drop the "bar" sign from the time constants τ_1 and τ_2.

2.5 Voltage response to sinusoidal input currents: impedance amplitude and phase

The voltage response of a neuron receiving an oscillatory current input at a frequency f can be characterized by its amplitude (normalized by the input amplitude) and phase (or phase-shift). Together, these quantities constitute the so called impedance function $Z(f)$ (a complex quantity). For simplicity, here we use the term impedance, and we use the notation $Z(f)$, to refer to the impedance amplitude. We refer to the graphs of $Z(f)$ and $\phi(f)$ as the impedance and phase profiles.

For a linear system receiving sinusoidal input currents of the form (3), the voltage response is given by

$$V_{out}(t; f) = A_{out}(f) \, \sin\left(\Omega \, t + \phi(f)\right) \tag{35}$$

where $A_{out}(f)$ is the voltage amplitude. The impedance amplitude is given by

$$Z(f) = \frac{A_{out}(f)}{A_{in}}. \tag{36}$$

When the input and output frequencies coincide, as it always happens for linear systems, the phase $\phi(f)$ captures the difference between the peaks of the voltage output and input current normalized by the oscillation period. Eqs. (57)-(58) in the Appendix give the analytical expressions for the impedance and phase profiles.

9

2.5.1 Impedance and phase profiles for 2D linear systems: resonance and phasonance

For 2D linear systems the impedance profiles are either a decreasing function of f (red curve in Fig. 1-a1), representing a low-pass filter response, or a non-monotonic graph exhibiting a peak Z_{max} at a non-zero input frequency (blue curve in Fig. 1-a1) representing a resonant response at the (resonant) frequency f_{res}. The phase profile may be either an increasing function of f converging asymptotically to $\phi = \pi/2$ (red curve in Fig. 1-a2), and representing a delayed response for all values of f, or a non-monotonic graph exhibiting a zero-phase response at a non-zero input frequency f_{phas} (blue curve in Fig. 1-a2) that we refer to as the phasonant frequency. For $f = f_{phas}$ the input current and output voltage peak at the same time. For $f < f_{phas}$, the voltage response is advanced, while for $f > f_{phas}$ the voltage response is delayed. We have investigated the mechanisms of generation of resonance and phasonance in 2D linear systems in [41].

2.5.2 Impedance and phase profiles for 3D linear systems: emergence of antiresonance and antiphasonance

For certain parameter regimes (discussed later in this paper) the voltage response for 3D linear systems is more complex than for 2D linear ones [2, 18] . The impedance profile may exhibit a trough Z_{min} at an (anti-resonant) input frequency $f = f_{ares}$ in addition to the peak at $f = f_{res}$ (Fig. 1-b1). The phase profile may have an additional zero-frequency cross at $f = f_{aphas}$ (antiphasonance) in addition to the one at $f = f_{phas}$ (Fig. 1-b1). For $f = f_{aphas}$ and $f = f_{phas}$ the input current and output voltage peak at the same time. The voltage response is delayed for $f < f_{aphas}$ and $f > f_{phas}$ and advanced for f satisfying $f_{phas} < f < f_{aphas}$.

2.5.3 Attributes of the impedance and phase-profiles

The investigation of the role of resonant and amplifying currents requires the tracking of changes in both the impedance and phase profiles as a certain model parameter changes. It is helpful to characterize these graphs by using a small number of attributes (Fig. 1) that capture the salient properties of their shapes. Some of these attributes have been defined earlier: f_{res}, f_{phas}, f_{ares}, f_{aphas}, Z_{max} and Z_{min}. When $f_{ares} = 0$, $Z_{min} = Z_0$ ($= Z(0)$).

In addition, we will use the resonance amplitude $Q_Z = Z_{max} - Z_{min}$ and the antiresonance amplitude $Q_0 = Z_{max} - Z_0$. In the absence of antiresonance, $Q_Z = Q_0$. The half-width frequency band $\Lambda_{1/2}$ is the length of the frequency interval in between f_{res} and the input frequency value at which $Z(f) = Z_{max}/2$, and measures the system's selectivity to input frequencies in the resonant frequency band. We do not explicitly analyze this attribute in this paper.

3   Results

The investigation of the mechanisms of generation of resonance, phasonance, antiresonance and antiphasonance consists primarily of understanding how and under what conditions f_{res}), f_{phas}, f_{ares}) and f_{aphas} transition from zero to positive values respectively. Alternatively, resonance requires $Q_Z > 0$ and $Q_0 < Q_Z$ (for systems exhibiting resonance but not antiresonance $Q_Z = Q_0$).
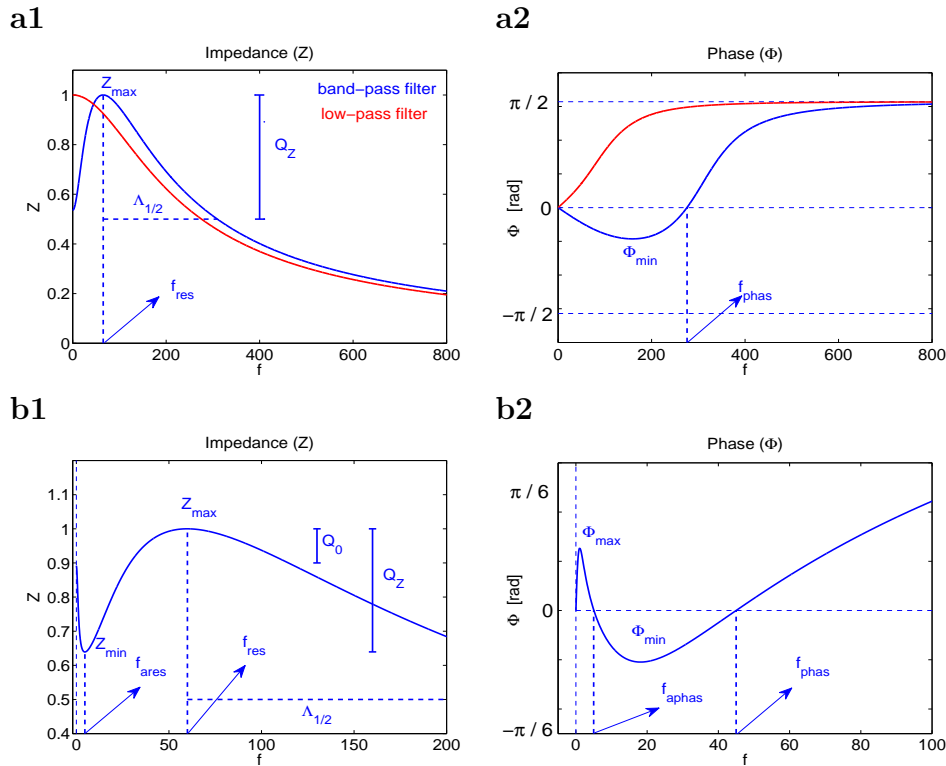
Figure 1: **Representative Impedance (Z) and phase (ϕ) profiles (curves of Z and ϕ vs. the input frequency f) for 2D (a) and 3D (a,b) linear systems.** **(a1)** The impedance Z is characterized by four attributes: the resonant frequency f_{res}, the impedance peak Z_{max}, the resonance amplitude $Q_Z = Z_{max} - Z(0)$, and the half-bandwidth $\Lambda_{1/2}$. **(a2)** The phase ϕ is characterized by two attributes: the zero-crossing frequency f_{phas} and the phase minimum ϕ_{min}. **(b1)** The impedance Z is characterized by additional attributes: the anti-resonant frequency f_{ares}, the impedance local minimum Z_{min} and $Q_0 = Z_{max} - Z_0$. The resonance amplitude is defined as $Q_Z = Z_{max} - Z_{min}$ and it coincides with the definition in panel a (in the absence of antiresonance $Z_{min} = Z_0$). **(b2)** The phase ϕ is characterized by two additional attributes: the phase local maximum ϕ_{max} and the zero-crossing phase f_{aphas} on the descending portion of ϕ.

If a neuron exhibits resonance, the mechanisms of amplification of the voltage response in the resonant frequency band consist primarily of understanding how the resonance amplitude Q_Z and the maximal impedance Z_{max} increase as certain model parameter increases. These two attributes convey different information about the voltage response in the resonant frequency band. This is particularly important for neurons, since Q_Z may increase (decrease), while Z_{max} decreases (increases), thus bringing the voltage further away from (closer to) the threshold for spike generation in the resonant frequency band.

3.1 Mechanisms of generation of resonance and phasonance in 2D linear systems revisited

3.1.1 Biophysical mechanisms

In [3,41] we identified the basic mechanisms of generation of resonance for the two-dimensional linear system (4)-(5) with $g_2 = 0$ (henceforth, the 2D system). Additionally, we carried a thorough analysis of the properties of the attributes of the voltage response and their dependence on the linearized conductances, g_L and g_1, and the time constant $\bar{\tau}_1$. One lesson from these studies is that resonance and phasonance involve the complex interaction not only between the linearized conductances, but also the effective time scales. We revisit these results here and we refer the reader to [3,41,42] for a more detailed discussion.

Resonance in 2D linear systems can be created by three fundamental mechanisms involving: (i) an increase in g_1, (ii) an increase in g_L, and (iii) an increase in $\bar{\tau}_1$. Relevant aspects of the dependences of the main attributes of the voltage response (f_{res}, f_{phas}, Z_{max} and Z_0) with these parameters are summarized in Fig. 2.

For $g_1 = 0$, $f_{res} = f_{phas} = f_{nat} = 0$ and $Z_{max} = Z_0$ ($Q_Z = 0$). As g_1 increases above certain threshold value, resonance is generated by an unbalanced decrease in Z_{max} and Z_0, which is more pronounced for Z_0 (Fig. 2-b1). This threshold value for g_1 depends on both g_L and $\bar{\tau}_1$. The 2D system may exhibit resonance, phasonance and intrinsic oscillations. If this happens, f_{res}, f_{phas} and f_{nat} are increasing functions of g_1 (Fig. 2-a1).

The ability of the 2D system to exhibit resonance for $g_L = 0$ depends on the values of both g_1 and $\bar{\tau}_1$. For the example in Fig. 2 the 2D system exhibits resonance for $g_L = 0$. While f_{res} is an increasing function of g_L, f_{phas} is independent of g_L and f_{nat} is a decreasing function of g_L for a significantly large range of values of g_L (Fig. 2-a2). Resonance is amplified by a combined increase in both Z_{max} and Z_0 as g_L decreases, which is significantly more pronounced for Z_{max} (Fig. 2-b2). While resonance is still present for large values of g_L, Q_Z decreases very fast as g_L increases and approaches zero. This attenuation of the voltage response constitutes an effective annihilation of the resonance phenomenon.

The monotonic behavior of the resonance amplitude Q_Z is not necessarily associated with a specific monotonic behavior of f_{res} and f_{phas}. In fact, f_{res} increases with increasing values of g_1, but it first increases and then decreases with increasing values of g_L (Fig. 2-a).

The mechanism of generation of resonance by increasing values of $\bar{\tau}_1$ (and fixed values of both g_1 and g_L) involves an increase in Z_{max}, while Z_0 remains unchanged (Fig. 2-a2 and -b2). This amplification of the voltage response (compare the solid- and dashed-blue curves in Fig. 2-b) is accompanied by a decrease in f_{res}, f_{phas} and f_{nat} (compare the corresponding solid and dashed curves in Fig. 2-a).
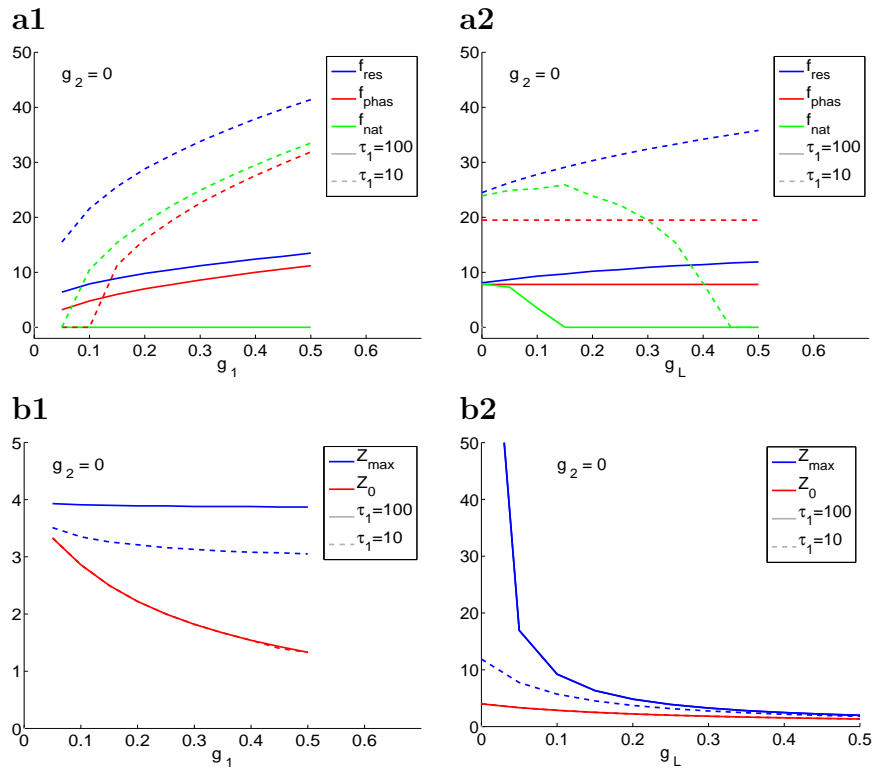
12

Figure 2: **Attributes of the voltage response for the 2D system (4)-(6) with $g_2 = 0$ for representative parameter values.** **(a)** f_{res}, f_{phas} and f_{nat} as a function of g_1 for $g_L = 0.25$ (a1) and as a function of g_L for $g_1 = 0.25$ (a2). **(b)** Z_{max} and Z_0 as a function of g_1 for $g_L = 0.25$ (b1) and as a function of g_L for $g_1 = 0.25$ (b2). The superimposed red-solid and red-dashed curves indicate that Z_0 is independent of τ_1. We used the following parameter values $C = 1$ and $A_{in} = 1$.

13

3.1.2 Dynamic mechanisms

For the 2D system ($g_2 = 0$), the properties of the voltage response to sinusoidal inputs result from the interplay of the cell's intrinsic time scales and the input's time scale. From (26)-(27) with $g_2 = 0$, the former is determined by the effective time constants $C\,g_L^{-1}$ and $\bar{\tau}_1^{-1}$. The latter is determined by the input frequency f. The time scale separation between v and w_1 is given by $C\,g_L^{-1}\bar{\tau}^{-1}$. The parameter g_1 (or $g_1\,g_L^{-1}$) controls the strength of the negative feedback.

For $f \to 0$, the cell response is instantaneous regardless of the values of the time constants. The voltage v is slaved to the current input. Therefore, the voltage maximum value is equal to the cell's resistance ($Z(0) = Z_0 = (g_L + g_1)^{-1}$) and the voltage and the input peak at the same time, so $\phi(0) = 0$ (e.g., Figs. 3-a and -b). For very large values of f, on the other extreme, the voltage response is very slow as compared to the input's speed. The voltage reaches very small extreme values and peaks with a delay approaching $\pi/2$. In the limit of $f \to \infty$, regardless of the values of the time constants, the voltage response is zero (Figs. 3-a and -b).

Resonance occurs if for an intermediate frequency range $Z(f) > Z_0$, while phasonance requires the voltage response to be able to peak before the sinusoidal input (advanced response) for a range of input frequencies [41]. In both cases, the cell's response is optimal at $f = f_{res}$ and $f = f_{phas}$, respectively, in the sense that it is neither too fast nor too slow to reach a maximum value and to peak in-phase with the input respectively. This requires appropriate combinations of the dimensionless parameters $g_1\,g_L^1$ and $C\,g_L^{-1}\bar{\tau}^{-1}$ such that the former is large enough and the latter is small enough.

3.1.3 The dynamic phase-plane

All this is better captured by the rescaled 2D model (30)-(31) with $\kappa = 0$ (henceforth the 2D model) and the dynamic phase-plane approach we used in [41] (see also [42] for an extension to 2D nonlinear systems). Fig. 3-c shows the superimposed voltage traces for representative input frequencies f (see panels a and b) during one cycle for the linear 2D model with a sinusoidal input of the form (3) for a representative value of A_{in}. The black curve is a caricature of the sinusoidal input whose peak time serves as the phase reference ($\phi = 0$).

Fig. 3-d shows the projection of the phase-space (for v, w and t) onto the v-w plane (henceforth the phase-plane) with the superimposed limit cycle response (LCR) trajectories corresponding to the voltage response curves for the input frequencies shown in Fig. 3-c. For clarity, we show the envelope-plane diagram without the LCR trajectories in Fig. 3-e.

We view the nullcline for the autonomous 2D model as the baseline for the analysis. As t progresses, this v-nullcline moves cyclically, parallel to itself in between the two red-dashed lines corresponding to $I_{in,1} = A_{in}$ (top) and $I_{in,1} = -A_{in}$ (bottom). Clearly, the distance between the moving v-nullcline and the baseline v-nullcline is equal to A_{in}.

3.1.4 Envelope-plane diagrams and envelope curves

The black dots in the LCR trajectories in Fig. 3-d note the points for which they reach their maximum v-values. As f increases these points span the blue curves, which we refer to as the upper and lower *envelope-curves* [41]. We refer to the diagrams such as these in Fig. 3-e, containing the v-nullclines (solid and dashed), the w-nullcline and the envelope-curves, as the *envelope-plane diagrams*.

Envelope-plane diagrams contain geometric and dynamic information about a system's frequency response to oscillatory inputs, and are the frequency analogous to phase-plane di-

agrams [41]. Trajectories in the envelope-plane diagrams (upper and lower envelopes) are curves parameterized by the input frequency as trajectories in the phase-planes are curves parametrized by time. (Neither f nor t are explicit in these diagrams.) The cusp ("horizontal peak") in the envelope curve corresponds to the peak in the impedance profile, and hence it corresponds to $f = f_{res}$. The point on the envelope-plane curve tangent to the upper dashed-red line corresponds to $f = f_{phas}$ since this tangency indicates that both the limit cycle trajectory and the v-nullcline reach their maximum at the same time.

The shape of the limit cycle trajectories depend on the interaction between the input frequency f and the underlying vector field [41]. We use this framework to explain the representative cases discussed above for the 2D linear system (30)-(31) (with w_1 substituted by w and $\kappa = 0$)

3.1.5 Quasi-one dimensional dynamics for low values of the input frequency f

For values of $f \ll 1$ both equations are very fast ($dv/dt \to \infty$ and $dw/dt \to \infty$), and therefore the RLC trajectories track the motion of the fixed-point almost instantaneously (in a quasi-steady-state fashion). In the limit $f \to 0$, the RLC trajectory moves cyclically along the w-nullcline in between the fixed-points generated by the dashed-red lines (intersection between these lines and the w-nullcline). The v-coordinate of this fixed-point is equal to $(1+\alpha)^{-1}A_{in}$. For slightly higher values of f, such as $f = 1$, the RLC trajectories become elliptic-like around the w-nulcline, reflecting the emergence of a horizontal (off w-nullcline) direction of motion.

3.1.6 Quasi-one dimensional dynamics for high values of the input frequency f

For large enough values of $f \gg 1$, both equations are very slow ($dv/dt \to 0$ and $dw/dt \to 0$), and therefore the RLC trajectory evolves with a very low speed relative to the motion of the v-nullcline. Therefore, the v-nullcline "comes back" while the RLC trajectory has only reached a very small distance from the fixed-point and is forced to reverse direction. As a result, the amplitude of the RLC trajectory is small as compared to other values of f (e.g., limit cycle trajectory for $f = 60$). In the limit $f \to \infty$, the amplitude of the RLC trajectory is zero (the limit cycle shrinks to the origin).

3.1.7 Two-dimensional dynamics for input frequencies in the resonant frequency band

For intermediate values of f there is a transition in the shapes of the RLC trajectories between these two limit cases. Specifically, they first widen as their major axes rotate clockwise, and then they shrink while their major axis remains almost horizontal. Geometrically, the system exhibits resonance if for at least one of these RLC trajectories it is satisfied that $v_{max}(f) > v_{max}(0)$ as in Fig. 3-d for $f = 6$ and $f = f_{res} = 12$. The latter corresponds to the peak of the envelope-plane curve (Fig. 3-e). The system exhibits phase-resonance if both the v-nullcline and a RLC trajectory reach the upper dashed-red line at exactly the same time, thus generating a tangency between the envelope-plane curve and the dashed-red v-nullcline (Fig. 3-e). For the parameters in Fig. 3-d, the points on the envelope-curve corresponding to f_{res} and f_{phas} are very close (Fig. 3-e, bottom), almost indistinguishable.

15

For the limiting cases ($f = 0$ and $f \to \infty$), the RLC trajectories are quasi one-dimensional. For intermediate values of f the RLC trajectories are neither too fast nor too slow, and then, while they are "left behind" by the moving v-nullcline, they can take advantage of the two-dimensional vector field without being constrained to move in quasi-one-dimensional directions. For the appropriate parameter values it is this degree of freedom that allows RLC trajectories to reach values of $v_{max}(f)$ larger than $v_{max}(0)$, and so to exhibit resonance.
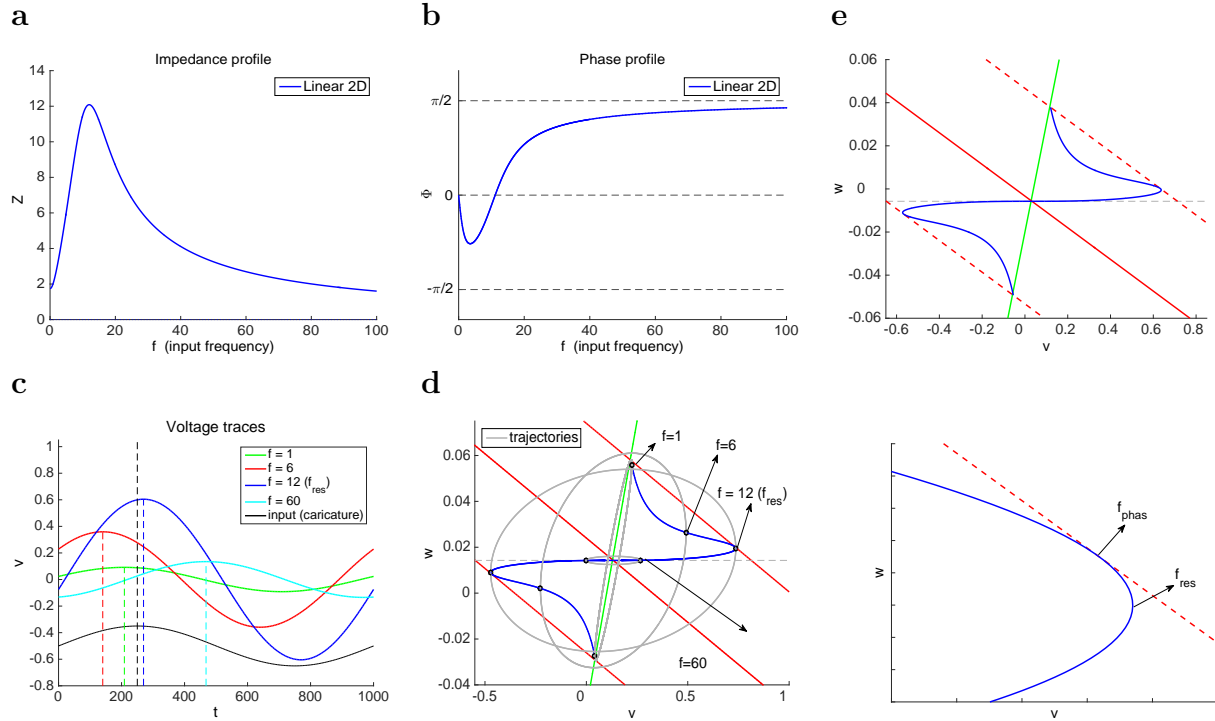
Figure 3: **Resonance and phasonance in 2D linear models.** (a) Impedance profile ($f_{res} = 12$). (b) Phase profile ($f_{phas} = 11.1$). The natural frequency is $f_{nat} = 10$. (c) Voltage traces for representative input frequency values. All curves are rescaled to have the same period (1000 ms). A caricature of the sinusoidal input (black curve) is included for reference below the curves. The dashed vertical lines note the peaks of the corresponding functions. The zero-phase response is indicated by the dashed-black vertical line (peak of the sinusoidal input). (d) Envelope-plane diagram. The red and green lines are the v- and w-nullclines respectively. The v-nullcline (solid-red) moves cyclically in between the displaced v-nullclines for $\pm A_{in}$ (dashed-red) following the sinusoidal input. The gray curves are the response limit cycle response trajectories corresponding to the voltage traces in panel c. The upper and lower envelope curves (solid blue curves) join the maximum (upper) and minimum (lower) points respectively on the response limit cycle response trajectories as f increases from $f = 0$ (intersection between the dashed-red and green lines) to $f \to \infty$ (intersection between the solid-red and green lines determining the fixed-point). Because of linearity, the upper and lower envelope-curves are symmetric with respect to the fixed-point. (e) "Clean" envelope-plane diagram. The v-coordinates of the envelope-curve are $Z A_{in}$. The maximum value of v on the envelope curve corresponds to $f = f_{res}$. The point on the envelope curve tangent to the upper dashed-red line corresponds to $f = f_{phas}$. The bottom panel is a magnification of the top one.

3.2   Resonance and phasonance in 3D linear systems: limiting and special quasi-2D cases

The results for the 2D system described above can be used to explain the dynamics of the 3D linear system in three special cases for τ_2: (i) $\tau_2 \to 0$ (w_2 has instantaneous dynamics), (ii) $\tau_2 \to \infty$ (w_2 has very slow dynamics), and (iii) $\tau_2 = \tau_1$ (w_1 and w_2 have identical dynamics). We assume that τ_1 is away from τ_2 in the first two cases.

In the first case, w_2 is slaved to v ($w_2 \sim v$) and, therefore, g_2 can be absorbed into g_L. A resonant (amplifying) gating variable will effectively increase (decrease) the value of g_L, and therefore attenuate (amplify) the voltage response and increase (decrease) the resonant frequency. The envelope-curve lives in the $w_1 = w_2$ plane (Fig. 4-b).

In the second case $\eta \to 0$. Provided that f is away from zero, w_2 has no dynamics ($dw_2/dt \to 0$). From the frequency-dependent properties point of view, system (4)-(6) behaves effectively as the 2D system described in Section 3.1 whose resistance is given by

$$Z(0) = \frac{1}{g_L + g_1}. \tag{37}$$

However, the 2D reduction is no longer valid when $f < \eta$, and therefore, a frequency boundary layer is created in the vicinity of $f = 0$ where the dynamics are quasi-1D and $Z(0)$ is given by

$$Z(0) = \frac{1}{g_L + g_1 + g_2}. \tag{38}$$

In other words, as f decreases $Z(f) \to (g_L + g_1)^{-1}$, but $Z(0) = (g_L + g_1 + g_2)^{-1}$. As we will discuss later in the paper, the abrupt transition required by the continuity of the solution to match these two values as $f \to 0$ is the main component of the generation of antiresonance and antiphasonance. Away from this frequency band, the envelope-curve lives in the (horizontal) v -w_1 plane (Figs. 4-c and -d).

In the third case, after transients have disappeared $w_2 = w_1$, then the two terms $g_1 w_1 + g_2 w_2$ in eq. (4) can be combined into one with g_1 replaced by $g_1 + g_2$. A resonant (amplifying) gating variable x_2 will effectively increase (decrease) the resonant effect of w_1 and therefore increase (decrease) the resonant frequency and increase (decrease) the resonance amplitude. The envelope-curve lives in the $v = w_2$ plane (Fig. 4-a).

The resulting modulatory effects on the dynamics of he 2D system caused by values of $g_2 \neq 0$ are expected to persist for values of τ_2 away from these special cases, but close enough to them, where the dynamics is effectively quasi-2D. In the next Section we examine how changes in τ_2 affects the behavior of the the voltage response as its qualitative behavior transitions through the cases discussed above.

3.3   Modulation and annihilation of existing resonances and emergence of antiresonance: basic biophysical mechanisms

Here we investigate the consequences of negative ($g_2 > 0$) and positive ($g_2 < 0$) feedback effects on the voltage response for the 3D system. We chose a 2D baseline system ($g_2 = 0$) in a parameter regime ($C = 1$, $g_L = 0.25$, $g_1 = 0.25$ and $\tau_1 = 100$) for which it exhibits both resonance and phasonance (blue curves in Fig. 5-a). We examine how changes in the linearized conductance g_2 affect the voltage response for $g_2 = 0$ for representative values of
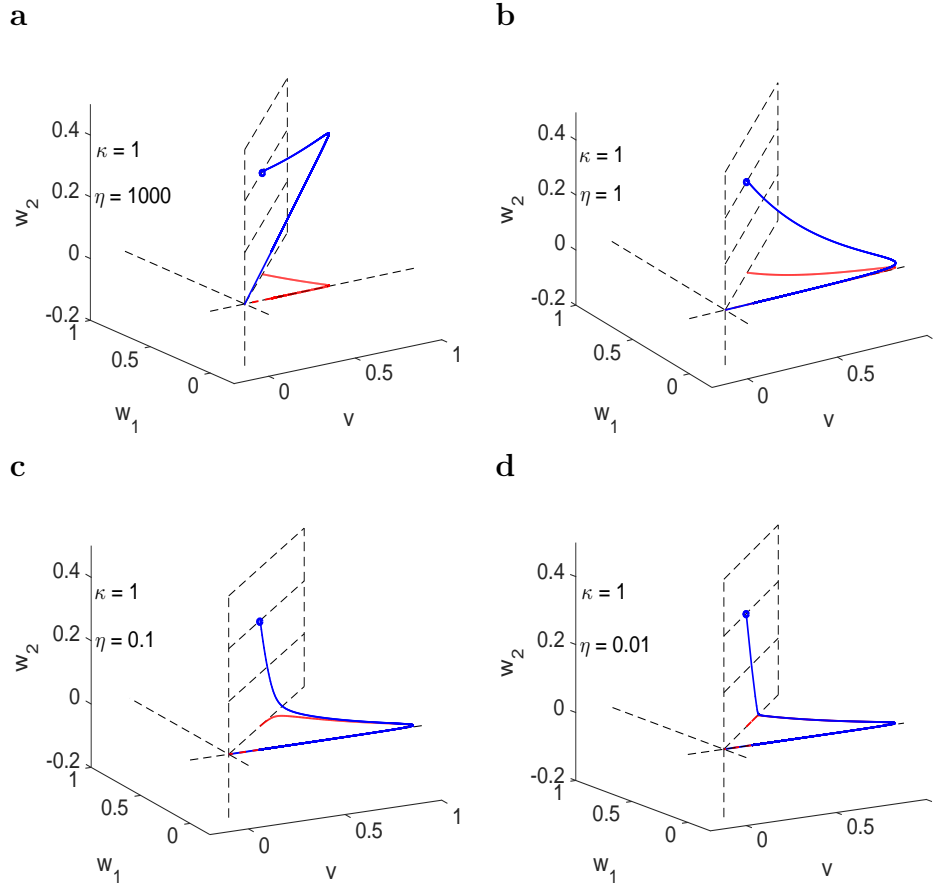
Figure 4: **Envelope-space diagrams for the linear 3D model in the quasi-2D regimes.** The (upper) envelope curves (solid blue) join the maximum points of the response limit cycle response trajectories as the input frequency f increases from $f = 0$ (blue dot on the w_1-nullsurface) to $f \to \infty$ (at the origin). The red curves are the projection of the envelope-curves onto the v-w_1 (horizontal) plane. The lower envelope curves (not shown) are symmetric to the upper ones with respect to the origin (fixed-point of the autonomous system). We used the following parameter values: $\alpha = 1$, $\epsilon = 0.05$ and $\kappa = -1.2$. The dynamics become increasingly 2D as η decreases as indicated by the larger portions of the envelope-curves (blue) that are almost superimposed to their projections (red) onto the v-w_1 planes. **(a)** $\eta = 1000$. The envelope curve "'lives" in the $v = w_2$ plane. **(b)** $\eta = 1$. The envelope curve "'lives" in the $w_1 = w_2$ plane. **(c)** $\eta = 0.1$. The envelope curve "lives" in the v-w_1 plane, except for the zero frequency band. **(d)** $\eta = 0.01$. The envelope curve "lives" in the v-w_1 plane, except for the zero frequency band.

the time constant τ_2 that increases from the top to the bottom panels. These values have been chosen to be below and comparable to τ_1. We divided our study into two cases: (i) interaction between two negative feedback effects ($g_2 > 0$, Fig. 5), and (ii) interaction between a negative and a positive feedback effects ($g_2 < 0$, Fig. 6). In both the cooperative ($g_2 < 0$) and competitive ($g_2 < 0$) feedback cases the voltage response is affected in qualitatively different ways depending on the values of τ_2 (relative speed of the two processes). However, these differences are more pronounced for the latter.

3.3.1 Interaction between two negative feedback effects: modulation of the voltage response

The interaction between two negative feedback effects ($g_2 > 0$) modulates the voltage response without generating antiresonances (Fig. 5). The "direction" and properties of this modulation depends on the value of τ_2. When w_2 is fast ($\tau_2 = 0.1$, Fig. 5-a), an increase in g_2 causes a strong attenuation of the voltage response accompanied by slight changes in f_{res} and f_{phas}. This is expected from our previous discussion in Section 3.2. This attenuation involves a strong decrease in Z_{max} and a smaller decrease in Z_0.

In contrast, for larger values of τ_2, there is an amplification of the voltage response as g_2 increases that is caused by an increase in Q_z due to a smaller decrease in Z_{max} than in Z_0 (Figs. 5-b and -c). This is accompanied by increases in f_{res} and f_{phas}. These effects are more pronounced for $\tau_2 = 50$ ($< \tau_1$) (Fig. 5-b) than for $\tau_2 = \tau_1 = 100$ (Fig. 5-b). As τ_2 increases further, Z_{max} approaches a constant value (not shown) and so does Q_Z since Z_0 is independent of τ_2. As expected, the impedance and phase profiles for different values of g_2 almost coincide for larger values of f except in the lowest frequency band whose size decreases with increasing values of τ_2 (compare Figs. 5-b and -c).

From (38), an increase (decrease) in g_2 causes a decrease (increase) in Z_0. In a separate set of simulations we have considered combined changes in the values of g_1 and g_2 such that $g_1 + g_2$ remains constant ($g_1 + g_2 = 0.25$) and, therefore, Z_0 also remains constant. The results (not shown) are qualitatively similar to these presented here (Figs. 5 and 6). One difference is that the impedance and phase profiles coincide along these level sets for $\tau_2 = \tau_1 = 100$ and there is a small amplification of the voltage response as with increasing values of g_2 as τ_2 increases above $\tau_2 = 100$. This is not surprising since g_1 decreases as g_2 increases and the activation of w_2 is delayed as compared to w_1. This amplification of the voltage response is accompanied with small decreases in both f_{res} and f_{phas}.

3.3.2 Interaction between a slow negative and a relatively fast positive feedback effects: amplification of the voltage response

For low values of τ_2, an increase in $|g_2|$ produces a strong amplification of the voltage response (Fig. 6-a) and a slight decrease in f_{res} and f_{phas}. For larger values of $\tau_2 < \tau_1$ the amplification of the voltage response as $|g_2|$ increases is less pronounced than for $\tau_2 = 0.1$ (Fig. 6-b) and both f_{res} and f_{phas} decrease. The weaker amplification of the voltage response results from a smaller increase in Z_{max} and a larger increase in Z_0 as $|g_2|$ increases. This in turn results from the slower activation of the positive feedback. This trend continues as long as τ_2 is below τ_1.
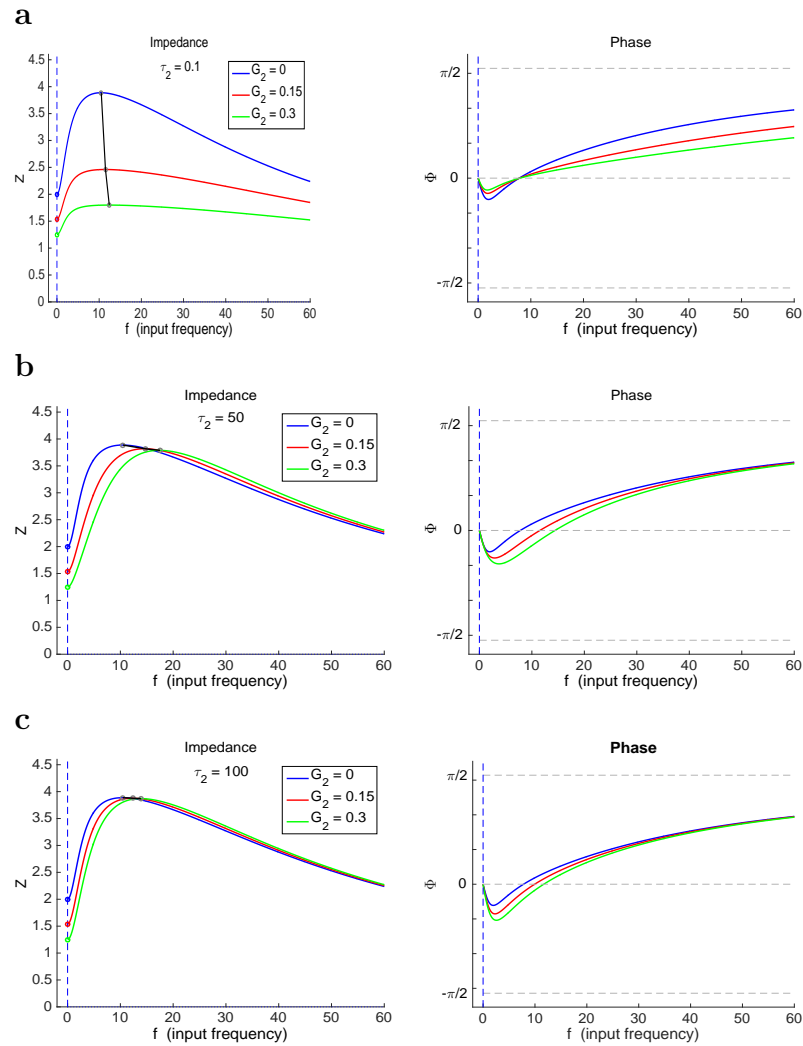
Figure 5: **Impedance and phase profiles for system (4)-(6) with $g_2 > 0$ (interaction between two resonant feedback effects) for representative sets of parameter values.** The gray lines in the left panels connect the peaks of the impedance profiles. We used the following parameter values $C = 1$, $g_L = 0.25$, $g_1 = 0.25$, $\tau_1 = 100$ and $A_{in} = 1$.

3.3.3 Interaction between negative and positive feedback effects with comparable slow dynamics: annihilation of resonance

As τ_2 approaches τ_1 both resonance and phasonance are annihilated as g_2 decreases ($|g_2|$ increases) past a threshold value (Fig. 6-c). For the green curve in Fig. 6-c, the voltage response at non-zero frequencies is not fast enough to raise above Z_0 and, therefore, $Q_Z = 0$.

Note that the slower activation of the positive feedback renders the voltage response almost unaffected by increasing values of $|g_2|$ for values of f outside a small vicinity of $f = 0$ whose size decreases with increasing values of τ_2 (compare Figs. 6-b, -c and -d, left panels).

3.3.4 Interaction between a slow and a slower negative feedback effects: generation of antiresonance and antiphasonance

As τ_2 increases above τ_1, both antiresonance and antiphasonance emerge (Fig. 6-d). As for $\tau_2 = 100$ (Fig. 6-c), for $\tau_2 = 200$ (Fig. 6-d) the slower activation of w_2 renders the values of Z_{max} almost unaffected by increasing values of $|g_2|$. However, the interaction between a faster negative feedback and a slower positive feedback causes $Z(f)$ to decrease below Z_{max} before reaching this value. This antiresonance mechanism restitutes resonance. An analogous effect is observed in the phase profiles where antiphasonance emerges as $|g_2|$ increases for $\tau_2 > \tau_1$.

For values of g_1 and g_2 such that $g_1 + g_2$ remain constant (not shown), the picture does not qualitatively change for values of $\tau_2 < \tau_1$. For $\tau_2 = \tau_1 = 100$, the impedance and phase profiles coincide. antiresonance and antiphasonance still emerge for values of $\tau_2 = 200$, but both phenomena are much less pronounced that in the case described in the previous paragraphs.

3.4 The shaping of the attributes of the impedance and phase profiles by the complex interplay of g_2 and $\bar{\tau}_2$

Here we extend the results from the previous sections to provide a global picture of how changes in g_2 and τ_2 affect the voltage response of the 3D linear system to sinusoidal inputs. Our results are presented in Figs. 7 to 11 for the same set of baseline parameter values as in Figs. 5 and 6. The colormap diagrams code for the values attributes of the impedance and phase profiles in the g_2 - τ_2 parameter space for fixed-values of the baseline parameters. The other graphs in each figure correspond to representative curves of for these attributes as a function of τ_2 and g_2. In these graphs we include the corresponding curves for $\tau_1 = 10$ (dashed) in addition to the (baseline) $\tau_1 = 100$ (solid).

3.4.1 Dependence of the modulating effects of the resonant gating variable x_2 ($g_2 > 0$) on g_2 and τ_2

For values of $g_2 > 0$ the 3D system exhibits no antiresonances (Figs. 7-a and -b, showing that Q_Z and Q_0 are identical). The impedance and phase profiles are qualitatively similar to these for the 2D system. The presence of an additional resonant gating variable modulates the voltage response and the resonance and phasonance phenomena, though not always in obvious ways.

As discussed above, the effect of changes in the values of g_2 on the resonant properties of the 3D system depends on the values of τ_2 (Fig. 7-a). For large enough values of τ_2, increasing g_2 causes an increase in Q_Z, similarly to its dependence on g_1 described above. This dependence
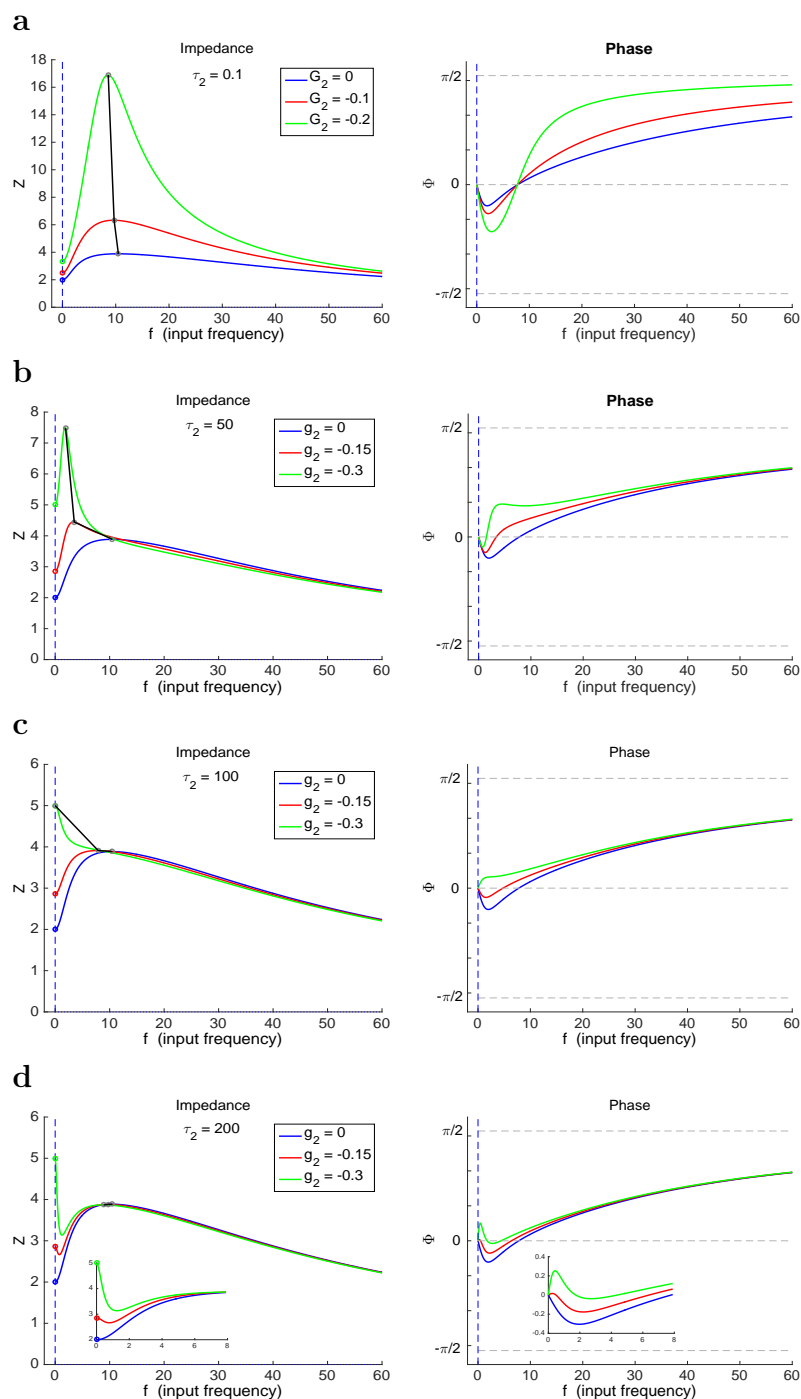
Figure 6: **Impedance and phase profiles for system (4)-(6) with $g_2 < 0$ (interaction between a negative and a positive feedback effects) for representative sets of parameter values.** The gray lines in the left panels connect the peaks of the impedance profiles. We used the following parameter values $C = 1$, $g_L = 0.25$, $g_1 = 0.25$, $\tau_1 = 100$ and $A_{in} = 1$.

is inverted for low values of τ_2: in the presence of a fast negative feedback, increasing g_2 causes an attenuation of the voltage response and a decrease in Q_Z.

3.4.2   The modulation mechanisms of the resonant gating variable x_2 $(g_2 > 0)$ depend on τ_1

We show this in Fig. 7-d. For large enough values of τ_1 (solid curves), the increase in Q_Z as g_2 increases results from a combined decrease in both Z_{max} and Z_0 , which is more pronounced for Z_0 than for Z_{max}. In contrast, for low enough values of τ_1 (dashed lines), Z_{max} remains constant as g_2 increases, while Z_0 decreases.

Increasing the value of τ_2 causes an amplification of the voltage response and an increase in Q_Z, which depend on the value of g_2. As τ_2 increases, the negative feedback effect provided by x_2 is slower, and therefore the voltage response can increase to higher values before this increase is opposed by x_2. This amplification is more pronounced for larger values of τ_1 (Fig. 7-c).
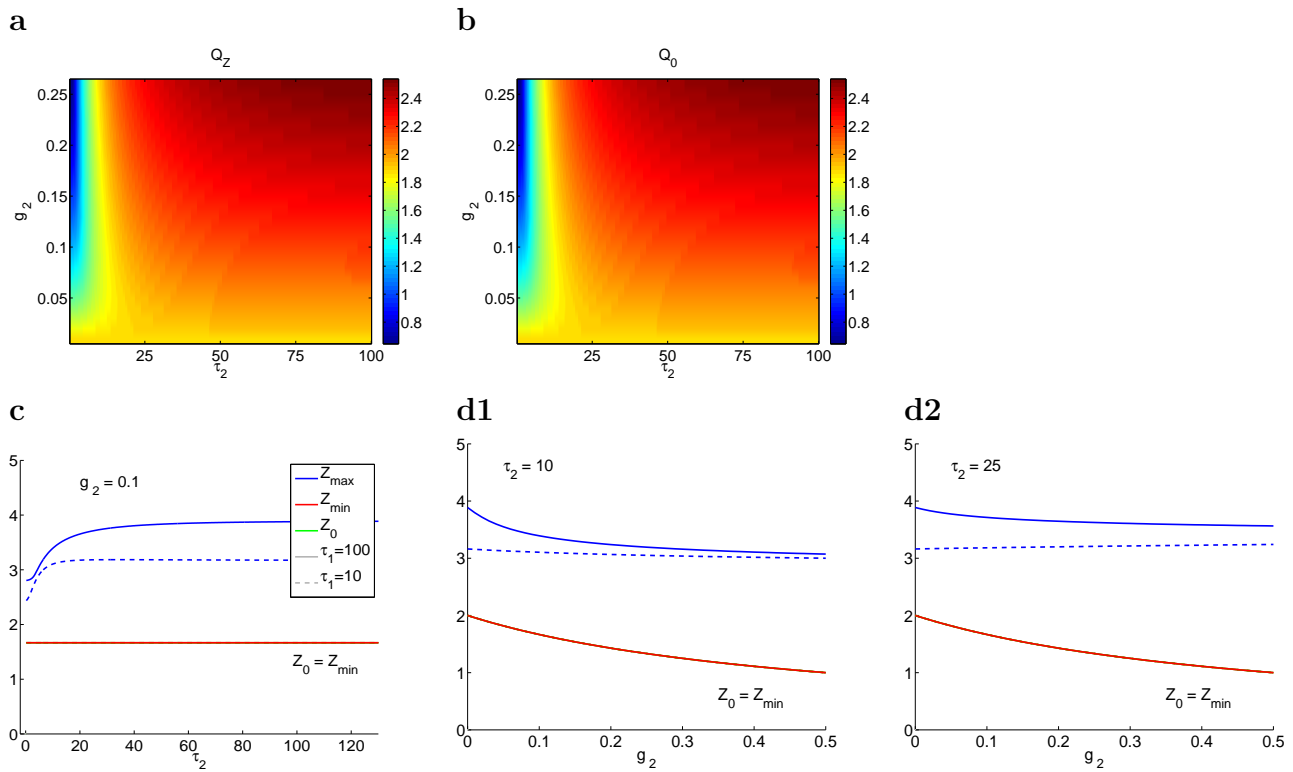

Figure 7: **Resonance amplitudes for system (4)-(6) with a resonant gating variable x_2 $(g_2 > 0)$ for a representative set of parameter values. Top panels (a, b):** Colormap diagrams for Q_Z (a) and Q_0 (b) in Gg_2 - τ_2 parameter space for $\tau_1 = 100$. **Bottom panels (c, d):** Representative curves of Z_{max}, Z_0 and Z_{min} as a function of τ_2 (c) and g_2 (d) for $\tau_1 = 100$ (solid) and $\tau_1 = 10$ (dashed). The superimposed red and green curves indicate that no antiresonances are present. The superimposed green-solid and green-dashed curves indicate that Z_0 (and Z_{min}) does not change with τ_2. We used the following parameter values $C = 1$, $g_L = 0.25$, $g_1 = 0.25$ and $A_{in} = 1$.

3.4.3   Increasing values of τ_2 generate bumps in the f_{res} and f_{phas} patterns

Both f_{res} and f_{phas} increase with increasing values of g_2 (Figs. 8-a and -b) with $f_{res} > f_{phas}$ (Fig. 8-d). Their values and rates of change depend on τ_2. Following our discussion in Section 3.2, their dependence can be thought of a transition from the values corresponding to $\tau_2 \to 0$ (2D system with g_L substituted by $g_L + g_2$) to the values corresponding to $\tau_2 \to \infty$ (2D system with $g_2 = 0$). This transition is non-monotonic and involves an increase in both f_{res} and f_{phas} for low enough values of τ_2 followed by a decrease as τ_2 continues to increase (Fig. 8-d). These properties of these "bumps" depend not only on the value of g_2 (Figs. 8-a and -b) but also on the value of the τ_1: the smaller τ_1 the stronger the bumps.
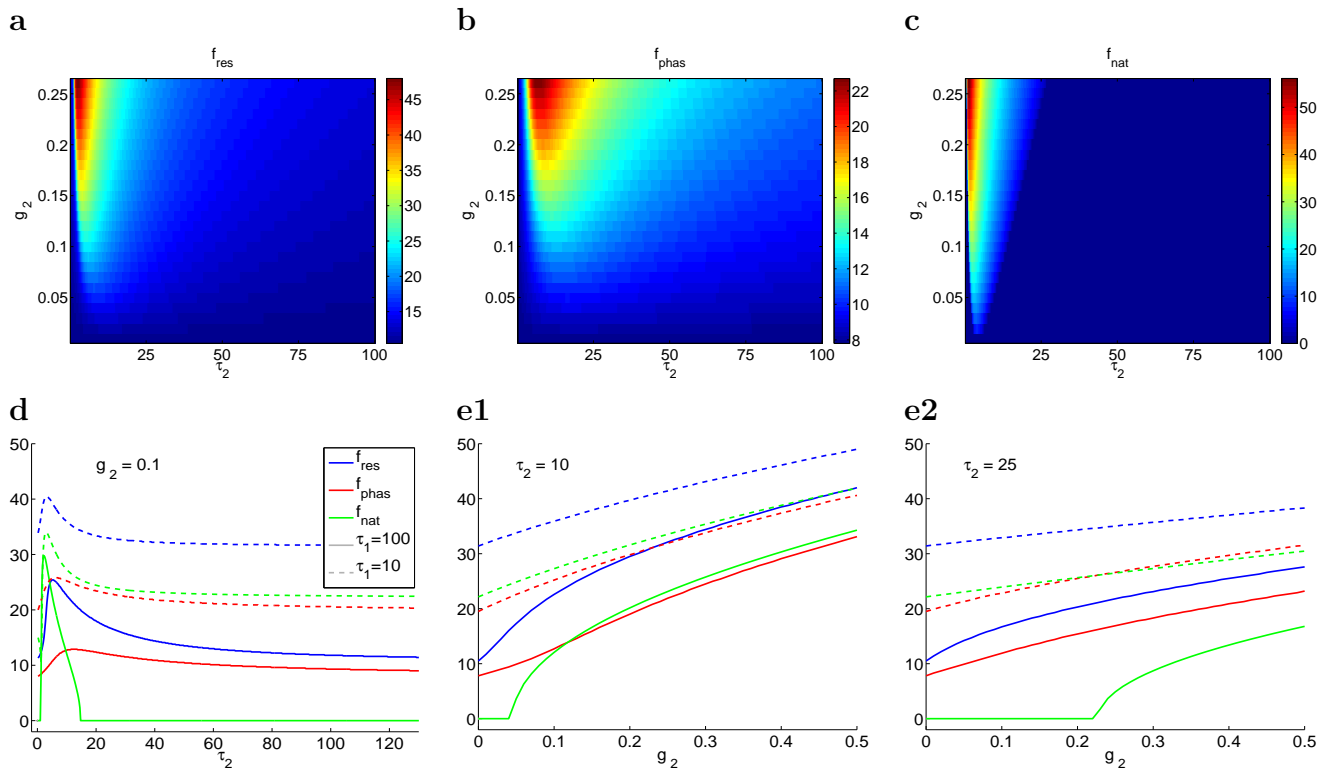

Figure 8: **Resonant, phasonant and natural frequencies for system (4)-(6) with a resonant gating variable x_2 ($g_2 > 0$) for a representative set of parameter values. Top panels (a, b, c):** Colormap diagrams for f_{res} (a), f_{phas} (b) and f_{nat} (c) in g_2 - τ_2 parameter space for $\tau_1 = 100$. **Bottom panels (d, e):** Representative curves of f_{res}, f_{phas} and f_{nat} as a function of τ_2 (d) and g_2 (e) for $\tau_1 = 100$ (solid) and $\tau_1 = 10$ (dashed). We used the following parameter values $C = 1$, $g_L = 0.25$, $g_1 = 0.25$ and $A_{in} = 1$.

3.4.4   Antiresonances are generated by the interplay of a slow resonant ($g_1 > 0$) and a slower amplifying ($g_2 < 0$)) gating variables

For values of $g_2 < 0$ antiresonance emerge provided τ_2 is large enough and g_2 negative enough (large enough in absolute value). This is reflected in the different colormap diagrams for Q_Z and Q_0 (Figs. 9-a and -b) in these parameter regimes. Figs. 9-d show the dependence of Q_Z

24

and Q_0 with g_2 for representative values of $\bar{\tau}_2$ and $\bar{\tau}_1$. Since Z_0 is independent of $\bar{\tau}_1$ and $\bar{\tau}_2$, the solid and dashed red curves ($\tau_1 = 100$ and $\tau_1 = 10$, respectively) coincide in panels c and d. In addition, the red and green curves coincide in panels d1 (left and right, respectively).

For $\tau_1 = 100$ and $\tau_2 = 100$ (panels d1, solid lines) $Z_{min} = Z_0$ ($Q_Z = Q_0$) for all values of g_2. In contrast, for $\tau_1 = 100$ and $\tau_2 = 200$ (panel d2, solid lines), the solid red (Z_0) and green (Z_{min}) curves separate as g_2 decreases, indicating the generation of antiresonances. Note that $Q_Z = Z_{max} - Z_0 < 0$ for the lowest values of g_2 in panel d2 (see also 6-d). For $\tau_1 = 10$ (dashed curves), the antiresonances emerge for lower values of τ_2 and higher values of g_2 (panels d, dashed curves, red-dashed and -solid curves are superimposed). These results show that the trade-off between currents for the generation of resonance does not only involve the conductances, voltage-dependencies and time scales associated to the amplifying gating variable but also the properties of the resonant gating variable x_1.
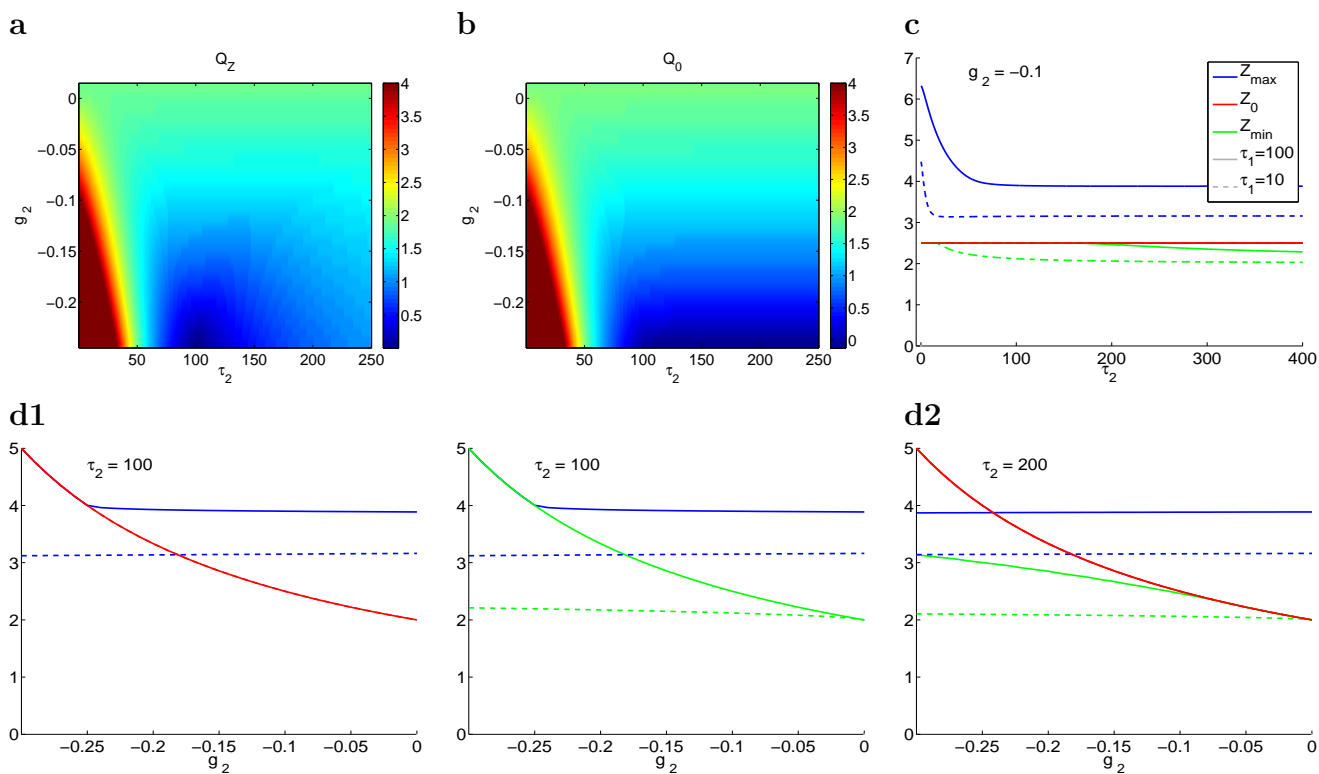

Figure 9: **Resonance amplitudes for system (4)-(6) with an amplifying gating variable x_2 ($g_2 < 0$) for a representative set of parameter values. Panels a, b:** Colormap diagrams for Q_Z (a) and Q_0 (b) in G_2 - τ_2 parameter space for $\tau_1 = 100$. **Panels c, d:** Representative curves of Z_{max}, Z_0 and Z_{min} as a function of τ_2 (c) and h_2 (d) for $\tau_1 = 100$ (solid) and $\tau_1 = 10$ (dashed). The superimposed red-solid and red-dashed lines indicate that Z_0 does not depend on τ_2. We used the following parameter values $C = 1$, $G_L = 0.25$, $G_1 = 0.25$ and $A_{in} = 1$.

3.4.5 f_{res} and f_{phas} decrease with decreasing values of $g_2 < 0$, but have a non-monotonic ("anti-bump-like") dependence with τ_2

Fig. 10 shows that both f_{res} and f_{phas} decrease with decreasing values of $g_2 < 0$ with rates that depend on the value of $\bar{\tau}_2$ (Fig. 10-a and -b). Similarly to the case $g_2 > 0$, the transition from $\bar{\tau}_2 = 0$ to $\bar{\tau}_2 \to \infty$ is non-monotonic and involves a decrease and subsequent increase in both f_{res} and f_{phas} in a relatively small range of values of $\bar{\tau}_2$. This range increases with decreasing values of $\bar{\tau}_1$ (compare the solid and dashed curves in Fig. 10-d for $\bar{\tau}_1 = 100$ and $\bar{\tau}_1 = 10$ respectively). The changes in the values of f_{res} and f_{phas} within these ranges are more pronounced for $\bar{\tau}_1 = 10$ (dashed curves) than for $\tau_1 = 100$ (solid curves) respectively. The dependence of f_{res} and f_{phas} with g_2 is monotonic (Fig. 10-e).
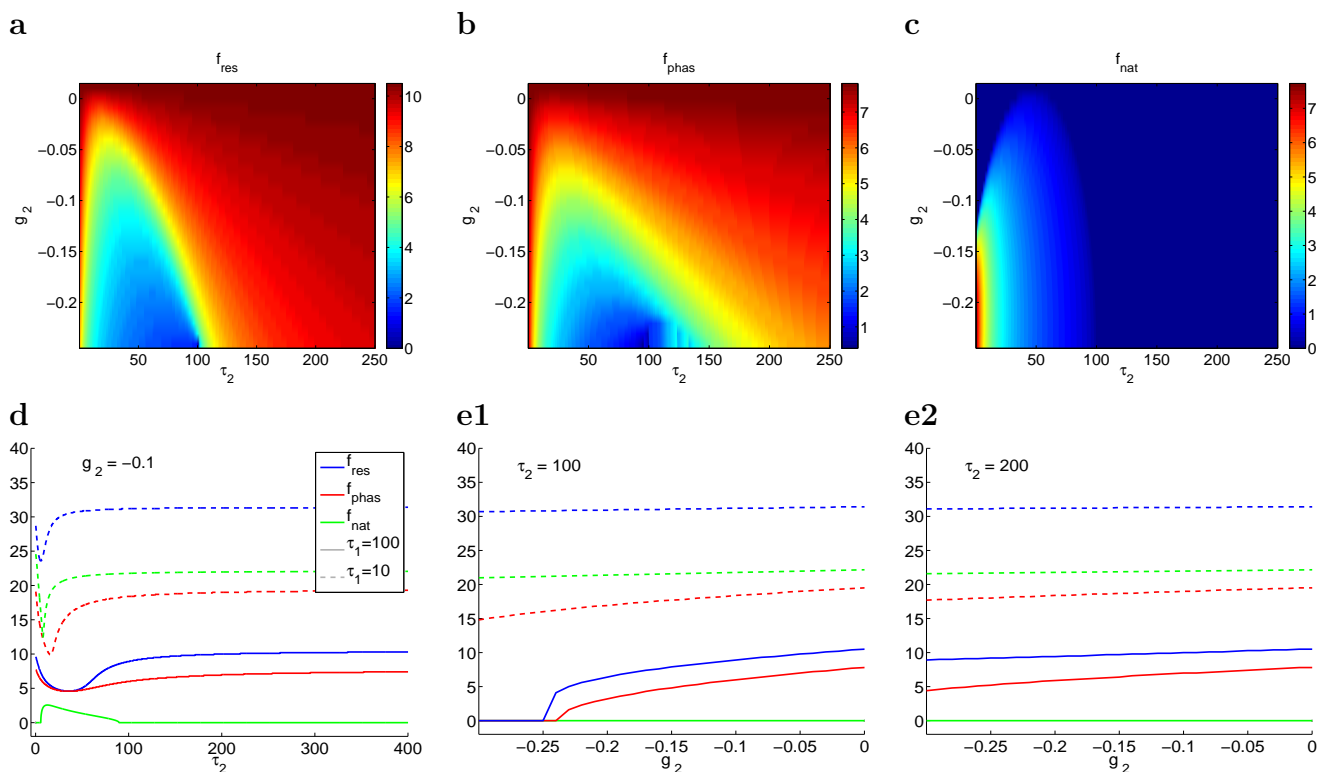

Figure 10: **Resonant, phasonant and natural frequencies for system (4)-(6) with an amplifying gating variable x_2 ($g_2 < 0$) for a representative set of parameter values. Top panels (a, b, c):** Colormap diagrams for f_{res} (a), f_{phas} (b) and f_{nat} (c) in g_2 - τ_2 parameter space for $\tau_1 = 100$. **Bottom panels (d, e):** Representative curves of f_{res}, f_{phas} and f_{nat} as a function of τ_2 (d) and g_2 (e) for $\tau_1 = 100$ (solid) and $\tau_1 = 10$ (dashed). We used the following parameter values $C = 1$, $g_L = 0.25$, $g_1 = 0.25$ and $A_{in} = 1$.

3.4.6 f_{ares} and f_{aphas} increase with decreasing values of $g_2 < 0$, but have a non-monotonic ("bump-like") dependence with τ_2

Fig. 11 illustrates the dependence of f_{ares} and f_{aphas} with g_2 and $\bar{\tau}_2$ for representative parameter values. Comparison between Figs. 11-a and -b shows that antiresonance may exist in the

absence of antiphasonance. Comparison between Figs. 11 and 10 shows that f_{ares} and f_{aphas} are always smaller than f_{res} and f_{phas}. Similarly to f_{res} and f_{phas}, f_{ares} and f_{aphas} are larger the smaller the values of $\bar{\tau}_1$. While typically $f_{res} > f_{phas}$, for a given set of parameter values, there are parameter regimes where $f_{ares} < f_{aphas}$ (Fig. 11–c, dashed curves). The dependence of f_{ares} and f_{aphas} with τ_2 is not necessarily monotonic and may exhibits "bumps" where these quantities first increase and then decrease. The dependence of f_{ares} and f_{aphas} with g_2 is monotonic, but f_{aphas} typically decrease faster than f_{ares} and these curves may intersect (Fig. 11-d).
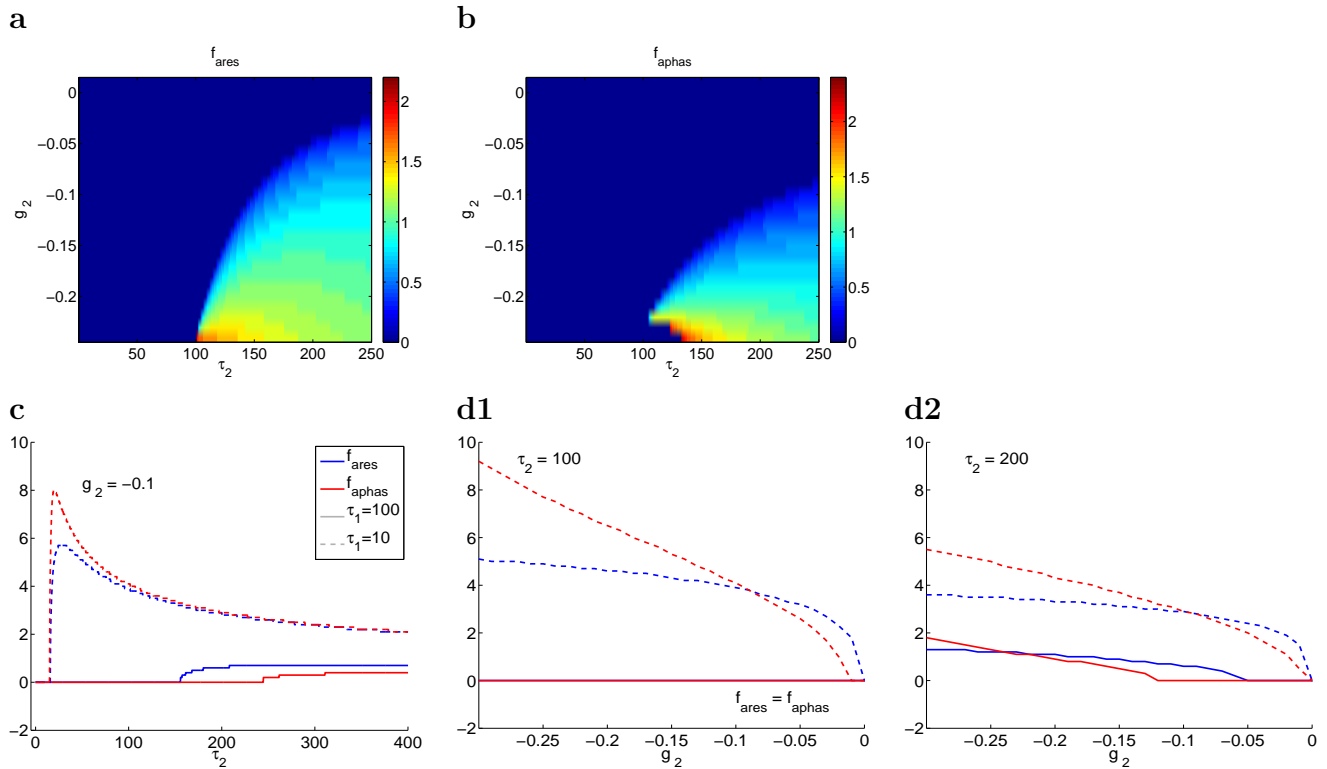

Figure 11: **Antiresonant and antiphasonant frequencies for system (4)-(6) with an amplifying gating variable x_2 ($G_2 < 0$) for a representative set of parameter values. Top panels (a, b):** Colormap diagrams for f_{ares} (a) and f_{aphas} (b) in g_2 - τ_2 parameter space for $\tau_1 = 100$. **Bottom panels (c, d):** Representative curves of f_{ares} and f_{aphas} as a function of τ_2 (c) and g_2 (d) for $\tau_1 = 100$ (solid) and $\tau_1 = 10$ (dashed). In panel d1, $f_{res} = f_{aphas} = 0$. We used the following parameter values $C = 1$, $g_L = 0.25$, $g_1 = 0.25$ and $A_{in} = 1$.

3.5 Dynamic mechanisms of generation of antiresonance and antiphasonance

Here we extend the analysis of 2D linear systems introduced in Section 3.1 to explain the mechanisms of generation of antiresonance and antiphasonance in the 3D linear system. We use the rescaled model (30)-(32) introduced in Section 2.3.2 (geometric rescaling). From our discussion in Section 3.4.4 and Fig. 6 (see also Section 3.2) antiresonance occurs when (i) x_1

is resonant ($g_1 > 0$), and (ii) x_2 is amplifying ($g_2 < 0$) and slower than x_1 ($\tau_2 < \tau_1$). Assuming $g_L > 0$, this yield $\alpha > 0$ and $\kappa < 0$. We will focus on the transition of η from $\eta > 1$ ($\tau_2 > \tau_1$) to $\eta < 1$ ($\tau_2 < \tau_1$) as we did in Fig. 4. We will use parameter values similar to the ones used in the previous sections: $\alpha = 1$ and $\epsilon = 0.05$.

As discussed above and shown in Fig. 6, one immediate consequence of the presence of the second amplifying gating variable ($\kappa < 0$) is an increase in the cell's resistance, given by

$$Z(0) = \frac{1}{1 + \alpha\,(1 + \kappa)}. \tag{39}$$

This has different consequences depending on the values of η and κ: resonance amplification (Fig. 6-b), resonance annihilation (Fig. 6-c) and generation of antiresonance/antiphasonance (Fig. 6-d).

3.5.1   Envelope-space diagrams: projections onto the v-w_1 and v-w_2 planes

In analogy to the sinusoidally forced 2D models discussed in Section 3.1.2, we view the dynamics of the oscillatory forced 3D model (30)-(32) as the result of the RLC trajectory tracking the oscillatory motion of the v-nullsurface

$$N_{v,t}(v) = -v - \kappa\,w_2 + A_t, \tag{40}$$

where A_t representes the oscillatory input (29), in between the levels corresponding to $A_{250} = 1$ and $A_{750} = -1$. The w_1- and w_2-nullsurfaces are both given by the same expression

$$N_{w_1}(v) = N_{w_2}(v) = \alpha\,v, \tag{41}$$

and are independent of the oscillatory input.

In order to facilitate the visualization of this "moving phase-space" we look at its projections onto the v-w_1 and v-w_2 planes, which we refer to simply as the envelope-plane diagrams (Fig. 12). The corresponding v-nullclines are given by

$$N_{v,1} = -v \qquad \text{and} \qquad N_{v,2} = -\frac{v}{\kappa}, \tag{42}$$

and the associated "moving v-nullclines" are given by

$$N_{v,1,t} = -v + A_t \qquad \text{and} \qquad N_{v,2,t,} = \frac{-v + A_t}{\kappa}. \tag{43}$$

We refer to the projections of the w_1- and w_2-nullsurfaces as the w_1- and w_2-nullclines respetively.

We use the limiting 2D regimes presented in Fig. 12 as the baseline for our discussion. The w_1- envelope-plane diagrams shown in Fig. 13 (left) are extensions to 2D type shown in Fig. 3 (panels d and e) for the same parameter values as in Fig. Fig. 12-c. For $f = 0$ (blue dot) the envelope-curve (blue) is located at the intersection of the v- and w_1-nullclines, which reflects the fast dynamics of the RLC trajectory along the w_1-nullcline. As $f \to \infty$ the RLC trajectory approaches the origin. The points in the envelope curve for f_{res} and f_{phas} are the peak in the v-direction (f_{res}) and the tangency point between the envelope-curve and the dashed-red line (f_{phas}), reflecting the fact that the RLC trajectory and the v-nullcline reached their maximum levels at the same time. For $\eta = 0$ (Fig. 12-a) w_2 is a constant and therefore the envelope-curve (right panel) evolves along the v-direction and has no frequency-dependent

28

effect on the system. For $\eta = 1$ and $\kappa = 0$ (Fig. 12-b) w_2 and w_1 have identical dynamics and therefore the w_1- and w_2 envelope curves are identical. However, since $\kappa = 0$, w_2 is following v, but not feeding back onto its dynamics. According to eqs. (42) and (43) the v-nullcline in the right panel is vertical for all values of A_t.

In both cases (Figs. 12-a and -b), the evolution of the RLC trajectories with increasing values of f is as in Fig. 3-d. For $f = 0$ the RLC trajectory moves along the w_1-nullcline. As f increases the RLC trajectory becomes elliptic-like and the major axis rotates towards the v-(horizontal) direction as its length increases. As f continues to increase, the RLC trajectory begins to shrink and eventually shrinks to the fixed-point (origin) as $f \to \infty$. It is important to note that the rays connecting the origin with the points in the envelope-plane curve are not necessarily the major axis of the corresponding elliptic-like RLC trajectories.

The changes in shape (and the direction of the major axis) of the RLC trajectories as f increases result from the changes in the effective speed of the RLC trajectories as the balance between ϵ and f change in eq. (31). The smaller this quotient, the larger the horizontal component of the direction of motion. We refer the reader to [41] for a detailed discussion.

3.5.2 The envelope-plane diagram and RLC trajectories for w_1 and w_2 have different dependences with their time-scale separation η

Fig. 12-c illustrates how the shapes of the envelope-plane curves are affected by the relative speed η of w_1 and w_2 in the simplest cases in which the 2D system is effectively decoupled from w_2 ($\kappa = 0$), but the dynamics of w_2 is dependent on v. The evolution of the RLC trajectories in the v-w_1 plane (Fig. 13-a, left) is as described above , but the evolution of the RLC trajectories in the v-w_2 plane follows different "rules" (Fig. 13-c, right), which gives rise to the envelope curves with different shapes than in the left panel. First, for low values of f (e.g., $f = 0.5$) the RLC trajectory is wider for v-w_2 than for v-w_1. This is because the horizontal components of the direction of motion are (locally) larger for w_2 than for w_1 due to the smaller time constant of the corresponding equations. This, in turn causes the RLC trajectories' major axis to rotate faster for w_2 than for w_1 (compare the RLC trajectories for $f = 4$ in Fig. 13). Second, as f increases, the RLC trajectories in the v-w_2 plane first shrink (from $f = 0.5$ to $f = 4$), then expand ($f = 46$) and then shrinks again ($f = 400$). This is not only in contrast to the behavior of the RLC trajectories in the v-w_1 for this particular value of η, but also for other values (e.g., $\eta = 1$ in Fig. 12-b).

3.5.3 Resonance attenuation and annihilation by increasing levels of the amplifying gating variable with $\eta = 1$ result from effective 2D dynamics

In Section 3.3.2 we showed that when $\tau_2 = \tau_1 = 100$ (Fig. 6-b) decreasing negative values of g_2 cause first an attenuation of the voltage response and then the annihilation of resonance (see also Fig. 9-a and -d1). Here we demonstrate that this phenomenon is generally valid for comparable time constants as captured by $\eta = 1$ ($\tau_1 = \tau_2$).

Figs. 14-a1, -b1 and -c1 show the envelope-plane diagrams for the 3D linear system for three representative values of $\kappa < 0$ (decreasing from a to c) and $\eta = 1$. For $\kappa = 0$ this system exhibits resonance (Fig. 12-b) that results from the 2D linear mechanisms invesigated in [41] and mentioned above. As κ decreases the resistance $Z(0)$ increases according to (39) moving the blue dot up along the w_1- and w_2-nullclines in the corresponding envelope plane diagrams. Resonance is attenuated because the vertex of the envelope-plane curve remains
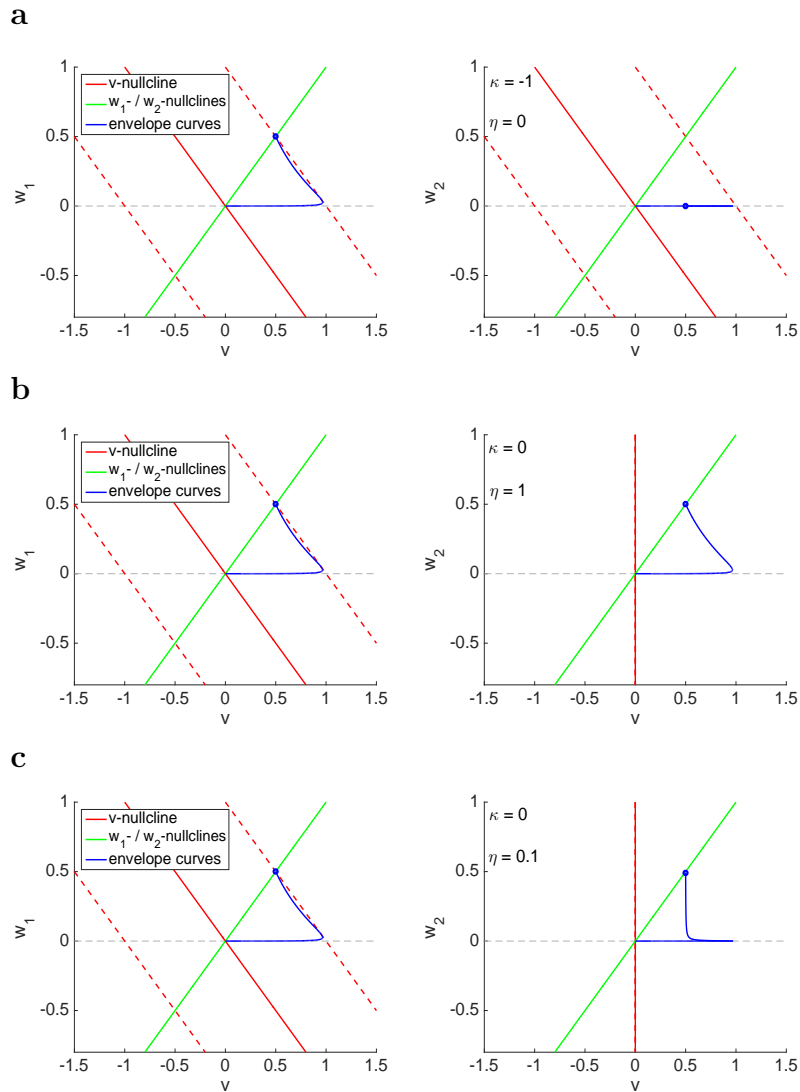
a

b

c

Figure 12: **Envelope-plane diagrams for the linear 3D model in the limiting 2D regimes.** The red and green nullclines are the projections of the v-, w_1- and w_2-nullsurfaces onto the v-w_1 (left) and v-w_2 (right) planes. The v-nullcline (solid-red) moves cyclically in between the displaced v-nullclines for $\pm A_{in}$ (dashed-red) following the sinusoidal input. The (upper) envelope curves (solid blue) join the maximum points of the projection of the limit cycle response trajectories onto the corresponding planes as the input frequency f increases from $f = 0$ (intersection between the dashed-red and green lines in the left panel) to $f \to \infty$ (intersection between the solid-red and green lines determining the fixed-point in the left panel). The lower envelope curves (not shown) are symmetric to the upper ones with respect to the origin (fixed-point of the autonomous system). **(a)** $\kappa = -1$ and $\eta = 0$. w_2 is constant and therefore has no frequency-dependent effect on the 3D system. **(b)** $\kappa = 0$ and $\eta = 1$. w_2 is decoupled from the 3D system. **(b)** $\kappa = 0$ and $\eta = 0.1$. w_2 is decoupled from the 3D system. We used the following parameter values: $\alpha = 1$ and $\epsilon = 0.05$.
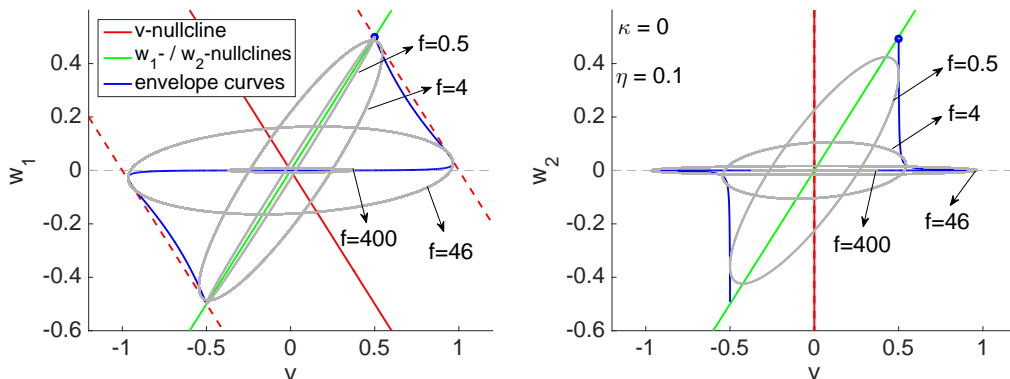
30

Figure 13: **Projections of the envelope-space diagram onto the v-w_1 and v-w_2 planes and representative response limit cycle trajectories for the linear 3D model in the limiting 2D regimes.** The paramter values correspond to Fig. 12-c.

almost fixed and therefore the angle between the two portions of the envelope-plane curve increases (Fig. 14-a1). As κ continues to increase this angle reaches ninety degrees, thus annihilating resonance (Fig. 14-b1 and -c1).

Key to this mechanism is the fact that the envelope-curves' vertices remain almost unchanged with changing values of κ. The primary reason for that is Quasi-2D dynamics for $\eta = 1$ discussed in Section 3.2 (Fig. 4-b) and also illustrated in Fig. 17-b for $\kappa = -1.2$. More specifically, the two variables w_1 and w_2 are identical, and therefore the system is effectively 2D and governed by eqs. (33)-(34). Figs. 14-a2, -b2 and -c2 show the envelope-plane diagrams for the 2D system and the same values of κ as in the left (a1, b1 and c1) panels. The envelope curves in the 2D v-w planes and the 3D projections onto the v-w_1 and v-w_2 planes are almost identical.

As explained in [41], for 2D linear systems the envelope-plane curve remains inside the triangle bounded by the w-nullcline, the horizontal v-axis and the displaced v-nullcline (dashed-red). The first two are independent of κ, while the latter experiences a change in slope from negative (Fig. 14-a2) to positive (Fig. 14-c2) as κ increases, but not the v-intercept, thus preventing the envelope-plane curve to peak at higher values of v.

3.5.4 Phasonance annihilation

Phasonance is annihilated for the same reason since as κ decreases, the envelope-plane curve looses its ability to "touch" the displaced (dashed) v-nullcline and therefore the only tangent point between the envelope-curve and the displaced v-nullcline is the blue dot.

3.5.5 Generation of antiresonance and antiphasonance

In Sections 3.3.4 and 3.4.4 we have shown that antiresonance and antiphasonance emerge as the result of the interplay of a slow resonant gating variable ($g_1 > 0$) and a slower amplifying ($g_2 < 0$) gating variable (see Figs. 6-d and 9-d2). In terms of the geometric rescaling (Section 2.3.2), these differences in the signs of the linearized conductances and the time constants associated to w_1 and w_2 are given by $\kappa < 0$ and $\eta < 1$.
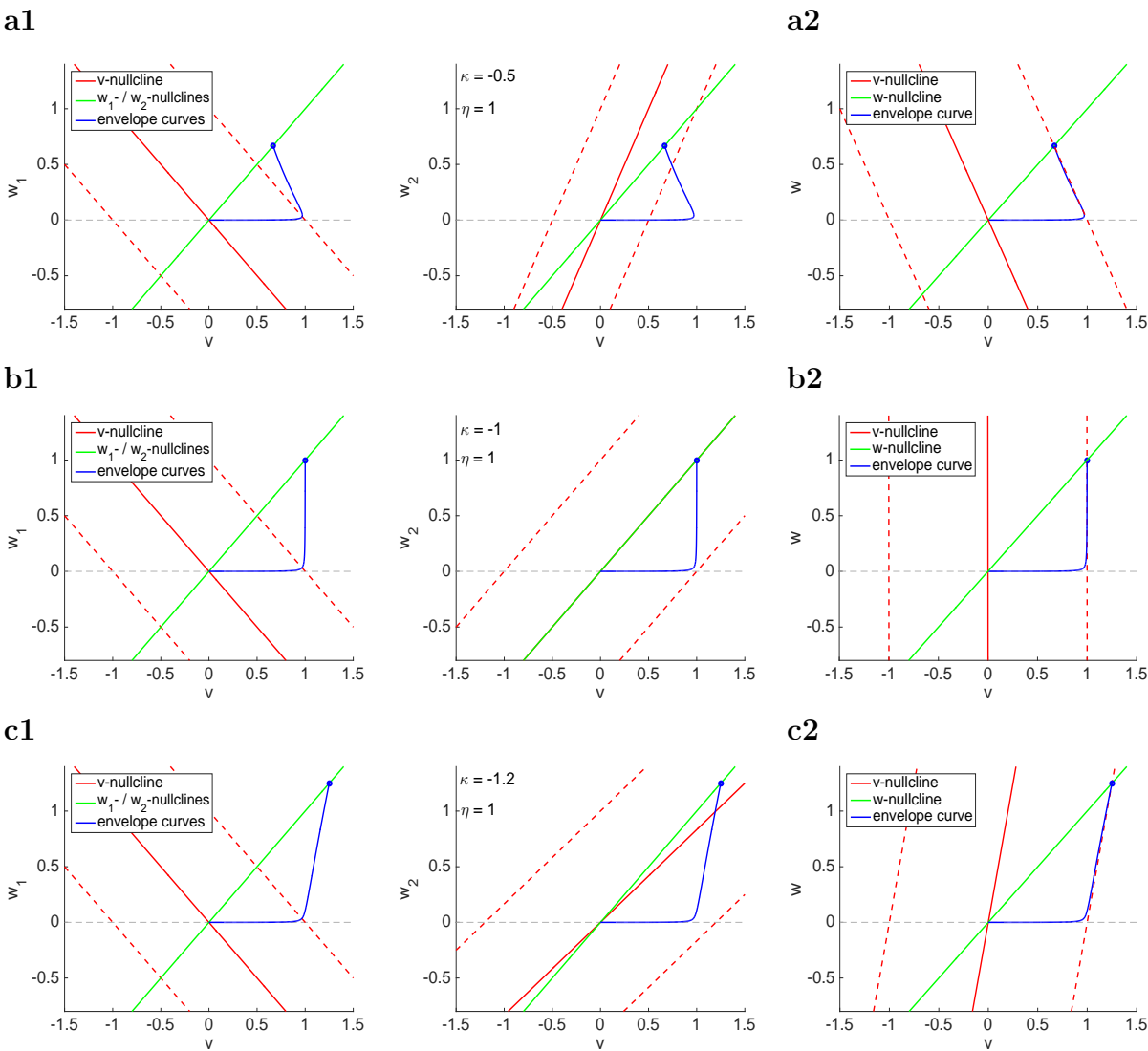
Figure 14: **Projections of the envelope-space diagrams for the linear 3D model with $\eta = 1$ (w_1 and w_2 have identical dynamics) on the v-w_1, v-w_2 and v-w planes.** The red and green nullclines are the projections of the v-, w_1- and w_2-nullsurfaces onto the v-w_1 (left) and v-w_2 (right) planes, respectively. The v-nullcline (solid-red) moves cyclically in between the displaced v-nullclines for $\pm A_{in}$ (dashed-red) following the sinusoidal input. The (upper) envelope curves (solid blue) join the maximum points of the projection of the limit cycle response trajectories onto the corresponding planes as the input frequency f increases from $f = 0$ (intersection between the dashed-red and green lines in the left panel) to $f \to \infty$ (intersection between the solid-red and green lines determining the fixed-point in the left panel). The lower envelope curves (not shown) are symmetric to the upper ones with respect to the origin (fixed-point of the autonomous system). Panels a2, b2 and c2 show the envelope-plane diagram for the equivalent 2D linear system (33)-(34). **(a)** $\kappa = -0.5$ and $\eta = 1$. **(b)** $\kappa = -1$ and $\eta = 1$. **(b)** $\kappa = -1..2$ and $\eta = 1$. We used the following parameter values: $\alpha = 1$ and $\epsilon = 0.05$.

Here we explain these phenomena in terms of the envelope-space diagrams (and their projections onto the v-w_1 and v-w_2 planes). Our results are presented in Figs. 15 and 16. In Fig. 15 we present the w_1- and w_2-envelope-plane diagrams for $\eta = 0.1$ and the same representative values of $\kappa < 0$ as in Fig. 14.

As discussed in Section 3.2 (Figs. 4-c and -d for $\kappa > 0$) for low enough values of $\eta < 1$ the dynamics of the 3D system is quasi-2D (v-w_1 plane) except for a boundary frequency layer in the vicinity of zero. This remains true for $\kappa < 0$ (Figs. 17-c and -d). Because of that, not only the horizontal portion of the envelope-curve remains almost unchanged as κ changes, but also a significant portion of the envelope-curve for the lower values of f along the displaced v-nullcline (dashed-red). In contrast, as for the $\eta = 1$ case explained above, decreasing values of κ cause $Z(0)$ to move up along the w_1- and w_2-nullclines.

Both antiresonance and antiphasonance are generated because the continuity of the solutions for changing values of f requires the envelope curve to decrease from $Z(0)$ to the v-$w-1$ plane at the level of the displaced v-nullcline (dashed-red) and then move along this v-nullcline towards the vertex of the triangular region. In doing so, $Z(f)$ reaches a minimum for $f_{ares} > 0$ before arriving to the maximum at the vertex ($f = f_{res}$) and ϕ "touches" the displaced v-nullcline twice: at the crossing point (f_{aphas}) on its way down and at the tangency point (f_{phas}). The behavior of the RLC trajectories for $\kappa = -1.2$ for representative values of f is shown in Fig. 16.

4 Discussion

In previous work we have investigated the biophysical and dynamic mechanisms of generation of subthreshold resonance and phasonance in 2D linear and linearized conductance-based models [3, 41] and in 2D conductance-based models with nonlinearities of quadratic type [42]. Resonance and phasonance in these models result from the interaction between positive and negative feedback effects provided by the passive (leak) current, a fast amplifying current (slaved to voltage) and a slower resonant current. Each of these currents was assumed to have a single gating variable, although the results are generally valid, at least at the linearized level. More recently, we have investigated how the interplay of positive and negative feedback effects with different time constants shape the intrinsic subthreshold oscillatory patterns in 3D linear and linearized conductance-based models having either two resonant gating variables or one resonant and one amplifying gating variables where the latter is not slaved to voltage and can be slower than the former [50]. These models may also include fast gating variables with instantaneous dynamics (slaved to voltage).

In this paper we have extended this work to include the response of 3D linear models to oscillatory inputs. Our goal was to understand how the cell's response patterns are shaped by the cooperative activity of the intrinsic feedback processes and time scales and the time scale of the external input determined by its frequency. These models have been studied previously in [2]. One lesson from these and previous studies, including our own, is that the frequency preference properties of cells in response to oscillatory inputs cannot necessarily be predicted from the cell's intrinsic oscillatory dynamics.

In addition to resonance and phasonance, which are also exhibited by the 2D models, the 3D models exhibit antiresonance and antiphasonance that require the extra degree of freedom provided the third gating variable. To our knowledge this is the first study that addressed the mechanism of generation of antiresonance and antiphasonance. For these phenomena to
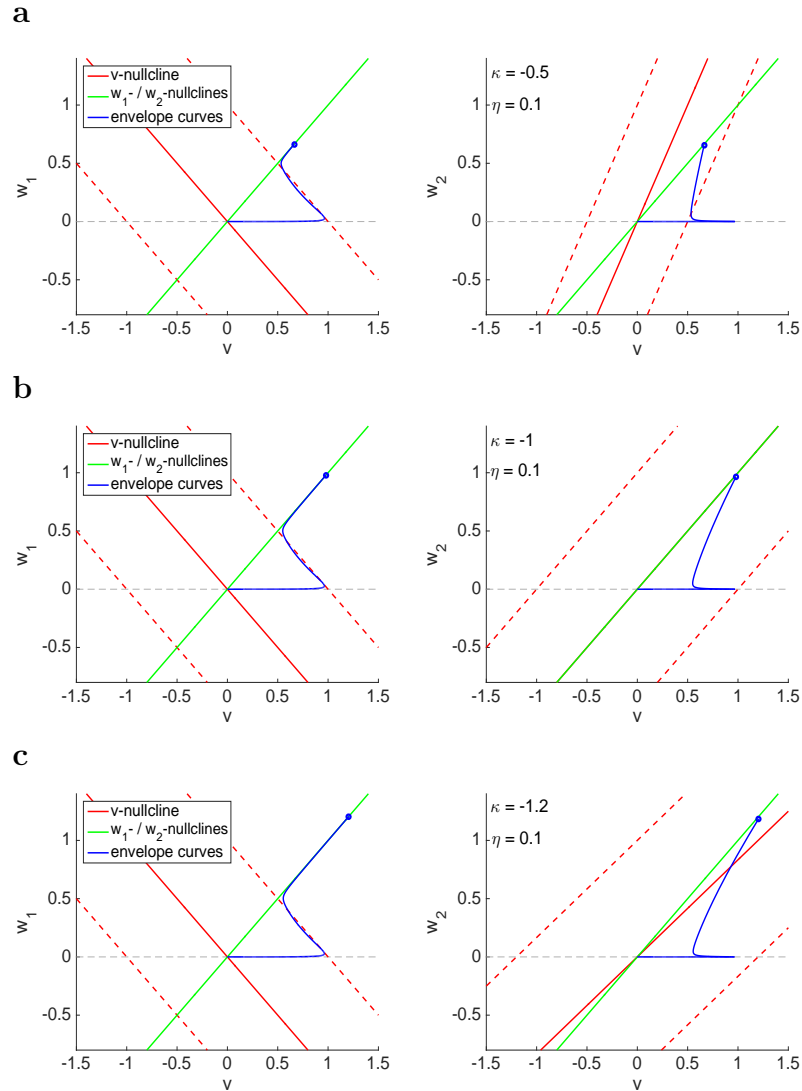
Figure 15: **Projections of the envelope-space diagrams for the linear 3D model onto the v-w_1 and v-w_2 planes in the limiting 2D regimes.** The red and green nullclines are the projections of the v-, w_1- and w_2-nullsurfaces onto the v-w_1 (left) and v-w_2 (right) planes. The v-nullcline (solid-red) moves cyclically in between the displaced v-nullclines for $\pm A_{in}$ (dashed-red) following the sinusoidal input. The (upper) envelope curves (solid blue) join the maximum points of the projection of the limit cycle response trajectories onto the corresponding planes as the input frequency f increases from $f = 0$ (intersection between the dashed-red and green lines in the left panel) to $f \to \infty$ (intersection between the solid-red and green lines determining the fixed-point in the left panel). The lower envelope curves (not shown) are symmetric to the upper ones with respect to the origin (fixed-point of the autonomous system). **(a)** $\kappa = -0.5$ and $\eta = 0.1$. **(b)** $\kappa = -1$ and $\eta = 0.1$. **(b)** $\kappa = -1.2$ and $\eta = 0.1$. We used the following parameter values: $\alpha = 1$ and $\epsilon = 0.05$.
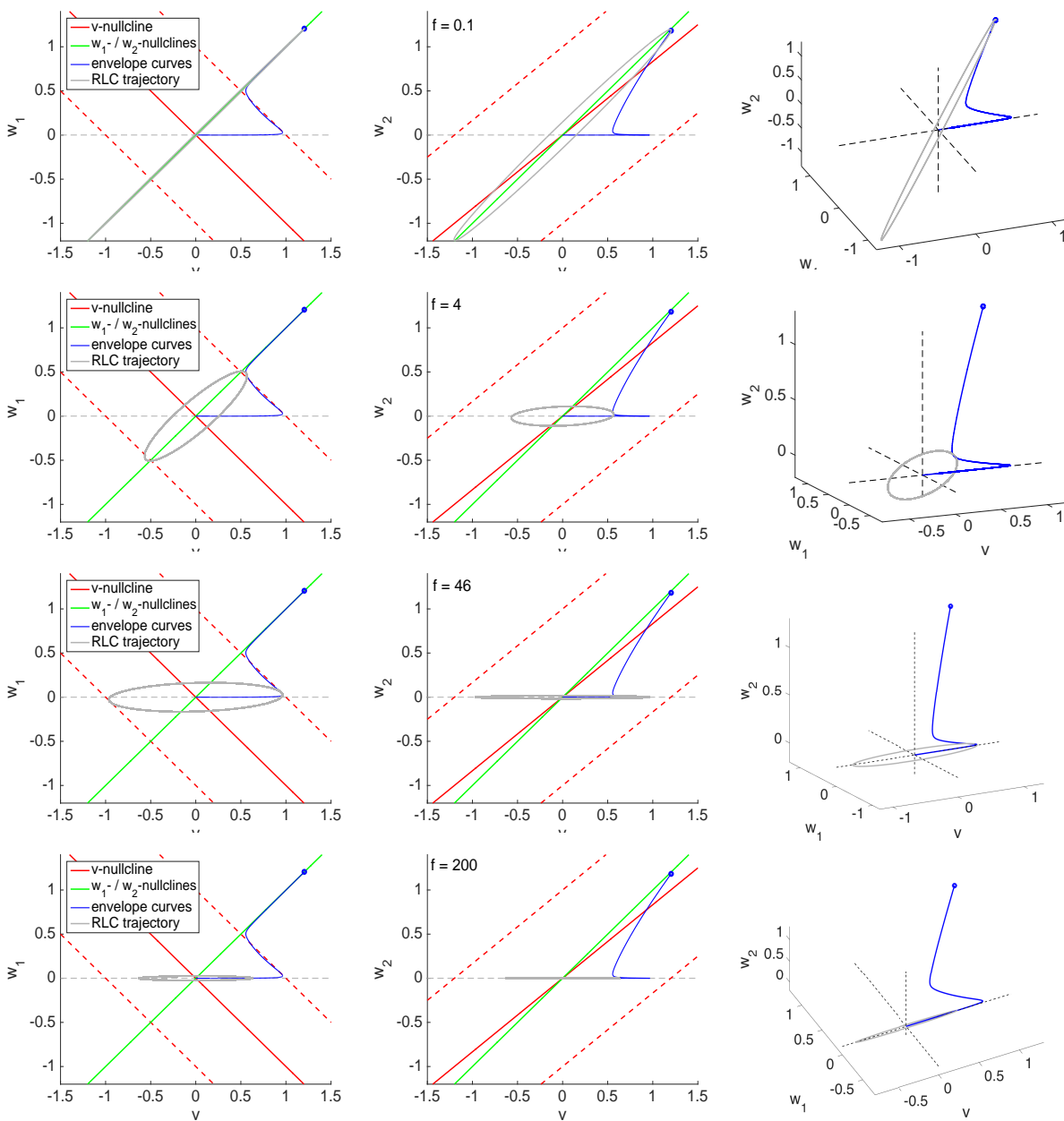
34

Figure 16: **Projections of the envelope-space diagrams onto the v-w_1 and v-w_2 planes (left and middle) and representative response limit cycle trajectories (right) for the linear 3D model in an antireso-nance regime.** The parameter values correspond to Fig. 15-c. The left and middle panels are the envelope-plane diagrams; i.e., the projections of the 3D envelope-space diagram onto the v-w_1 and v-w_2 planes with the superimposed projections of the RLC trajectories. The right panels show the 3D envelope-curve and the corresponding RLC trajectories.
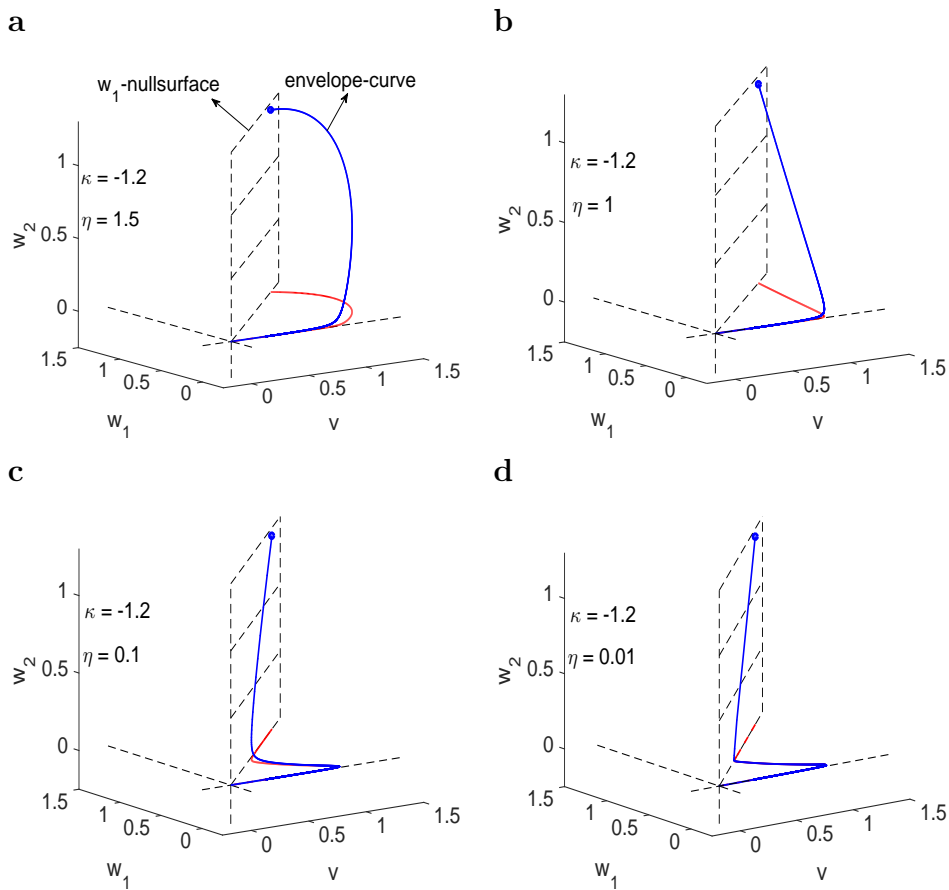
Figure 17: **Envelope-space diagrams for the linear 3D model: resonance modulation, annihilation and generation of antiresonance.** The (upper) envelope curves (solid blue) join the maximum points of the limit cycle response trajectories as the input frequency f increases from $f = 0$ (blue dot on the w_1-nullsurface) to $f \to \infty$ (at the origin). The red curves are the projection of the envelope-curves onto the v-w_1 (horizontal) plane. The lower envelope curves (not shown) are symmetric to the upper ones with respect to the origin (fixed-point of the autonomous system). We used the following parameter values: $\alpha = 1$, $\epsilon = 0.05$ and $\kappa = -1.2$. The dynamics become increasingly 2D as η decreases as indicated by the larger portions of the envelope-curves (blue) that are almost superimposed to their projections (red) onto the v-w_1 planes. **(a)** $\eta = 1.5$. Resonance is attenuated as η decreases. **(b)** $\eta = 1$. Resonance annihilation. **(c)** $\eta = 0.1$ Antiresonance and resonance **(d)** $\eta = 0.01$ Antiresonance and resonance.

occur one needs a resonant gating variable (x_1) with slow dynamics, so that the underlying 2D model exhibits resonance, and an amplifying gating variable (x_2) having both slower dynamics ($\tau_2 > \tau_1$). The stronger the linearized conductance g_2, the smaller the time constant τ_2 needed for these phenomena to occur (Fig. 11-a and -b). The occurrence of antiphasonance has similar requirements. In fact, there is a complex interplay of the magnitudes and effective time scales of the feedback processes that are responsible for either only modulating the voltage response of the underlying 2D system or creating the more complex types of impedance and phase profiles corresponding to antiresonance and antiphasonance.

Antiresonance has been experimentally reported in hippocampal interneurons [18] and, more recently, in the pyloric network LP neurons (crab stomatogastric ganglion) [37], and it has been shown to be present in the models discussed in [2]. To our knowledge, antiphasonance has not been experimentally reported yet. Our results predict that antiphasonance should occur under similar, but not identical, conditions as antiresonance. Testing the predictions of this study for the presence of both resonance and phasonance in biological neurons involves the manipulation of one or more ionic currents, including maximal conductances and time constants, and can be experimentally performed using the dynamic clamp technique [53–56]. Of particular relevance would be the determination of the differential roles played by different types of amplifying currents such as I_{Nap} (depolarization-activated) and I_{Kir} (hyperpolarization-activated) with slow dynamics in biological neurons having different types of resonant currents.

The impedance and phase profiles for linear systems can be computed analytically (see Appendix). These expressions are useful to generate graphs. However, because of their complexity, they provide little information and almost no insight into the dynamic mechanisms leading to the preferred response patterns in both amplitude and phase, including the roles played by the different effective time scales and their complex interaction. To address these issues we ave extended the envelope-space diagram approach introduced in [41, 42] to include the third variable, and we have constructed the envelope curves and their projections onto the appropriate planes. In addition to aid in the mechanistic analysis of the 3D linear system, this approach can be extended to the investigation of the preferred frequency responses to oscillatory inputs of nonlinear 3D systems where the analytic calculations are not possible.

Following previous work [41, 42] we rescaled time by the input frequency f in such a way that the sinusoidal input has frequency one for all values of f, which instead affect the speed of the voltage response (trajectories in the phase-space), but not the direction of the underlying vector field. By transforming f into a time constant factor we were able to capture the different balances that arise between f and the cell's intrinsic time constants as f changes. This, in turn, was functional in identifying the mechanism of generation of antiresonance and antiphasonance as an asymptotic boundary layer problem in the frequency domain. For large enough values of f, away from $f = 0$, the dynamics are quasi-2D and the impedance profile decreases as f decreases towards the boundary layer. In contrast, the resistance is controlled by the 3D system and is higher than this limit in the quasi-2D regime. The trough in the impedance profile is created because the continuity of the solution requires the impedance profile to connect the portions belonging to the two regimes. If in doing so the phase profile crosses the zero value, then antiphasonance is also generated.

For our simulations on the effects of g_2 and τ_2 on the cell's response patterns we used a baseline set of parameter values for the underlying 2D system (for v and x_1) such that it exhibits resonance in a regime where there are not intrinsic subthreshold oscillations. Our envelope-plane diagram analysis demonstrates that the results of our simulations have a more general

validity than the restricted considered scenarios. Additionally, as for the 2D models [41,42], this analysis shows that the mechanism of generation of resonance / phasonance and antiresonance / antiphasonance does not qualitatively depend on whether the fixed-point is a (stable) node or a focus. However, a detailed quantification of the dependence of the attributes of the impedance and phase profiles for the 3D linear system on the model parameters requires more research.

In [3, 42], for 2D conductance-based models we have shown through their linearization (or "quadratization") that changes in the levels of I_h (resonant, hyperpolarization-activated) and I_M (resonant, depolarization-activated) have opposite effects on the dependence of some of the attributes of the impedance and phase profiles (e.g., f_{res} and f_{phas}) on their maximal conductances when the levels of I_{Nap} were high enough, while these effects are qualitatively similar for the two resonant currents when the levels of I_{Nap} were lower. We hypothesize that these features of 2D models will also be present in 3D models and will extend to the antiresonance / antiphasonance attributes. Additional research is needed to test this both theoretically and experimentally and to determine whether additional differential properties emerge between the different types of resonant and amplifying currents.

Antiresonance can be viewed as a neuron's "anti-preferred" frequency response: a frequency selected by the neuron at which the voltage response is depressed or minimized. Our results indicate an alternative, but complementary view according to which the generation of antiresonance ($Q_Z > Q_0$) can operate as an additional mechanism of amplification of the voltage response in the resonant frequency band where both Z_{max} and Z_0 may remain unchanged as certain control parameter changes.

Our results open several questions about the neuron's response properties to oscillatory input. Further research is needed to extend these results to include the effects of the model nonlinearities, and the consequences of the presence of antiresonance and antiphasonance for spiking dynamics and network oscillations.

Acknowledgments

References

[1] B. Hutcheon and Y. Yarom. Resonance, oscillations and the intrinsic frequency preferences in neurons. *Trends Neurosci.*, 23:216–222, 2000.

[2] M. J. E. Richardson, N. Brunel, and V. Hakim. From subthreshold to firing-rate resonance. *J. Neurophysiol.*, 89:2538–2554, 2003.

[3] H. G. Rotstein and F. Nadim. Interaction between resonant and amplifying currents in two-dimensional neural models of frequency preference response to oscillatory input currents. *J. Comp. Neurosci.*, 37:9–28, 2014.

[4] I Lampl and Y. Yarom. Subthreshold oscillations and resonant behaviour: Two manifestations of the same mechanism. *Neuron*, 78:325–341, 1997.

[5] R. R. Llinás and Y. Yarom. Oscillatory properties of guinea pig olivary neurons and their pharmachological modulation: An *in vitro* study. *J. Physiol.*, 376:163–182, 1986.

[6] Y. Gutfreund, Y. Yarom, and I. Segev. Subthreshold oscillations and resonant frequency in guinea pig cortical neurons: Physiology and modeling. *J. Physiol.*, 483:621–640, 1995.

[7] I. Erchova, G. Kreck, U. Heinemann, and A. V. M. Herz. Dynamics of rat entorhinal cortex layer II and III cells: Characteristics of membrane potential resonance at rest predict oscillation properties near threshold. *J. Physiol.*, 560:89–110, 2004.

[8] S. Schreiber, I Erchova, U. Heinemann, and A. V. Herz. Subthreshold resonance explains the frequency-dependent integration of periodic as well as random stimuli in the entorhinal cortex. *J. Neurophysiol.*, 92:408–415, 2004.

[9] J. S. Haas and J. A. White. Frequency selectivity of layer II stellate cells in the medial entorhinal cortex. *J. Neurophysiol.*, 88:2422–2429, 2002.

[10] B. Hutcheon, R. M. Miura, and E. Puil. Subthreshold membrane resonance in neocortical neurons. *J. Neurophysiol.*, 76:683–697, 1996.

[11] P. Gastrein, E. Campanac, C. Gasselin, R. H. Cudmore, A. Bialowas, E. Carlier, L. Fronzaroli-Molinieres, N. Ankri, and D. Debanne. The role of hyperpolarization-activated cationic current in spike-time precision and intrinsic resonance in cortical neurons *in vitro*. *J. Physiol.*, 589:3753–3773, 2011.

[12] H. Hu, K. Vervaeke, and J. F. Storm. Two forms of electrical resonance at theta frequencies generated by M-current, h-current and persistent Na^+ current in rat hippocampal pyramidal cells. *J. Physiol.*, 545.3:783–805, 2002.

[13] H. Hu, K. Vervaeke, and J. F. Graham, L. J. Storm. Complementary theta resonance filtering by two spatially segregated mechanisms in CA1 hippocampal pyramidal neurons. *J. Neurosci.*, 29:14472–14483, 2009.

[14] R. Narayanan and D. Johnston. Long-term potentiation in rat hippocampal neurons is accompanied by spatially widespread changes in intrinsic oscillatory dynamics and excitability. *Neuron*, 56:1061–1075, 2007.

[15] R. Narayanan and D. Johnston. The h channel mediates location dependence and plasticity of intrinsic phase response in rat hippocampal neurons. *J. Neurosci.*, 28:5846–5850, 2008.

[16] B. Marcelin, A. Becker, M. Migliore, M. Esclapez, and C. Bernard. h channel-dependent deficit of theta oscillation resonance and phase shift in temporal lobe epilepsy. *Neurobiol. Dis.*, 33:436–447, 2009.

[17] E. D'Angelo, S. K. E. Koekkoek, P. Lombardo, S. Solinas, E. Ros, J. Garrido, M. Schonewille, and C. I. De Zeeuw. Timing in the cerebellum: oscillations and resonance in the granular layer. *Neuroscience*, 162:805–815, 2009.

[18] F. G. Pike, R. S. Goddard, J. M. Suckling, P. Ganter, N. Kasthuri, and O. Paulsen. Distinct frequency preferences of different types of rat hippocampal neurons in response to oscillatory input currents. *J. Physiol.*, 529:205–213, 2000.

[19] H. Tseng and F. Nadim. The membrane potential waveform on bursting pacemaker neurons is a predictor of their preferred frequency and the network cycle frequency. *J. Neurosci.*, 30:10809–10819, 2010.

[20] V. Tohidi and F. Nadim. Membrane resonance in bursting pacemaker neurons of an oscillatory network is correlated with network frequency. *J. Neurosci.*, 6427:6435, 2009.

[21] S. Solinas, L. Forti, E. Cesana, J. Mapelli, E. De Schutter, and E. D'Angelo. Fast-reset of pacemaking and theta-frequency resonance in cerebellar Golgi cells: simulations of their impact *in vivo*. *Frontiers in Cellular Neuroscience*, 1:4, 2007.

[22] N. Wu, C.-F. Hsiao, and S. H. Chandler. Membrane resonance and subthreshold membrane oscillations in mesencephalic V neurons: Participants in burst generation. *J. Neurosci.*, 21:3729–3739, 2001.

[23] R. Muresan and C. Savin. Resonance or integration? self-sustained dynamics and excitability of neural microcircuits. *J. Neurophysiol.*, 97:1911–1930, 2007.

[24] J. G. Heys, L. M. Giacomo, and M. E. Hasselmo. Cholinergic modulation of the resonance properties of stellate cells in layer II of the medial entorhinal. *J. Neurophysiol.*, 104:258–270, 2010.

[25] J. G. Heys, N. W. Schultheiss, C. F. Shay, Y. Tsuno, and M. E. Hasselmo. Effects of acetylcholine on neuronal properties in entorhinal cortex. *Frontiers in Behavioral Neuroscience*, 6:32, 2012.

[26] R. Zemankovics, S. Káli, O. Paulsen, T. F. Freund, and N. Hájos. Differences in subthershold resonance of hippocampal pyramidal cells and interneurons: The role of h-current and passive membrane characteristics. *J. Physiol.*, 588:2109–2132, 2010.

[27] M. F. Nolan, J. T. Dudman, P. D. Dodson, and B. Santoro. HCN1 channels control resting and active integrative properties of stellate cells from layer II of the entorhinal cortex. *J. Neurosci.*, 27:12440–12551, 2007.

[28] T. A. Engel, L. Schimansky-Geier, A. V. Herz, S. Schreiber, and I. Erchova. Subthreshold membrane-potential resonances shape spike-train patterns in the entorhinal cortex. *J. Neurophysiol.*, 100:1576–1588, 2008.

[29] A. Boehlen, U. Heinemann, and I. Erchova. The range of intrinsic frequencies represented by medial entorhinal cortex stellate cells extends with age. *J. Neurosci.*, 30:4585–4589, 2010.

[30] A. Boehlen, C. Henneberger, U. Heinemann, and I. Erchova. Contribution of near-threshold currents to intrinsic oscillatory activity in rat medial entorhinal cortex layer II stellate cells. *J. Neurophysiol.*, 109:445–463, 2013.

[31] R. K. Rathour and R. Narayanan. Inactivating ion channels augment robustness of sub-threshold intrinsic response dynamics to parametric variability in hippocampal model neurons. *J. Physiol.*, 590:5629–5652, 2012.

[32] R. K. Rathour and R. Narayanan. Homeostasis of functional maps in inactive dendrites emerges in the absence of individual channelostasis. *Proc. Natl. Acad. Sci. USA*, 111:E1787–E1796, 2014.

[33] D. Fox, H. Tseng, T. Smolinsky, H. G. Rotstein, and F. Nadim. Mechanisms of generation of membrane resonance in a bursting pacemaker neuron. *In review*, 2016.

[34] D. Fox, H. Tseng, H. G. Rotstein, and F. Nadim. Using multi-objective evolutionary algorithms to predict the parameters that determine membrane resonance in a biophysical model of bursting neurons. *BMC Neuroscience*, 15:79, 2014.

[35] D. Fox, H. Tseng, H. G. Rotstein, and F. Nadim. Membrane potential resonance of bursting neuron captured with an ICa/Ih biophysical model using multi-objective evolutionary algorithms. *Society for Neuroscience Abstracts*, 372.08:79, 2013.

[36] D. M. Fox, H.-A. Tseng, H. G. Rotstein, and F. Nadim. The role of a persistent inward current in shaping membrane resonance properties of different neuron types in an oscillatory network. *Society for Neuroscience Abstracts*, 215.06, 2014.

[37] D. M. Fox, H. G. Rotstein, and F. Nadim. Neuromodulation produces complex changes in resonance profiles of neurons in an oscillatory network. *Society for Neuroscience Abstracts*, 811.08, 2016.

[38] Y. Chen, Li., H. G. Rotstein, and F. Nadim. Membrane potential resonance frequency directly influences network frequency through gap junctions. *J. Neurophysiol.*, 116:1554–1563, 2016.

[39] J. Beatty, S. C. Song, and C. J. Wilson. Cell-type-specific resonances shape the response of striatal neurons to synaptic inputs. *J. Neurophysiol.*, 113:688–700, 2015.

[40] S. C. Song, J. A. Beatty, and C. J. Wilson. The ionic mechanism of membrane potential oscillations and membrane resonance in striatal lts interneurons. *J. Neurophysiol.*, 116:1752–1764, 2016.

[41] H. G. Rotstein. Frequency preference response to oscillatory inputs in two-dimensional neural models: a geometric approach to subthreshold amplitude and phase resonance. *J. Math. Neurosci.*, 4:11, 2014.

[42] H. G. Rotstein. Subthreshold amplitude and phase resonance in models of quadratic type: nonlinear effects generated by the interplay of resonant and amplifying currents. *J. Comp. Neurosci.*, 38:325–354, 2015.

[43] S. L. Schmidt, C. R. Dorsett, A. K. Iyengar, and F. Frölich. Interaction of intrinsic and synaptic currents mediate network resonance driven by layer V pyramidal cells. *Cereb. Cortex*, page DOI: 10.1093/cercor/bhw242, 2016.

[44] V. V. Moca, D. Nicolic, W. Singer, and R. Muresan. Membrane resonance enables stable robust gamma oscillations. *Cerebral Cortex*, 24:119–142, 2014.

[45] R. A. Tikidji-Hamburyan, J. J. Martínez, J. A. White, and C. Canavier. Resonant interneurons can increase robustness of gamma oscillations. *J. Neurosci. (in press)*, 35:15682–15695, 2015.

[46] E. Ledoux and Brunel N. Dynamics of networks of excitatory and inhibitory neurons in response to time-dependent inputs. *Front. Comp. Neurosci.*, 5:1–17, 2011.

[47] E. Stark, R. Eichler, L. Roux, S. Fujisawa, H. G. Rotstein, and G. Buzsáki. Inhibition-induced theta resonance in cortical circuits. *Neuron*, 80:1263–1276, 2013.

[48] L. S. Leung and H. W. Yu. Theta-frequency resonance in hippocampal CA1 neurons *in vitro* demonstrated by sinusoidal current injection. *J. Neurophysiol.*, 79:1592–1596, 1998.

[49] A. L. Hodgkin and A. F. Huxley. A quantitative description of membrane current and its application to conductance and excitation in nerve. *J. Physiol.*, 117:500–544, 1952.

[50] H. G. Rotstein. The shaing of intrinsic membrane potential oscillations: positive/negative feedback, ionic resonance/amplification, nonlinearities and time scales. *J Comp Neurosci (in press)*, 2016.

[51] H. G. Rotstein. Preferred frequency responses to oscillatory inputs in an electrochemical cell model: Linear amplitude and phase resonance. *Phys. Rev. E*, 88:062913, 2013.

[52] F. K. Skinner. Conductance-based models. *Scholarpedia*, 1:1408, 2006.

[53] A. A. Prinz, V. Thirumalai, and E. Marder. The functional consequences of changes in the strength and duration of synaptic inputs to oscillatory neurons. *J. Neurosci.*, 23:943–954, 2003.

[54] A. D. Jr. Dorval and J. A. White. Channel noise is essential for perithreshold oscillations in entorhinal stellate neurons. *J. Neurosci.*, 25:10025–10028, 2005.

[55] A. A. Sharp, M. B. O'Neil, L. F. Abbott, and E. Marder. The dynamic clamp: artificial conductances in biological neurons. *Trends Neurosci.*, 16:389–394, 1993.

[56] T. Kispersky, J. A. White, and H. G. Rotstein. The mechanism of abrupt transition between theta and hyperexcitable spiking activity in medial entorhinal cortex layer II stellate cells. *PLoS One*, 5:e13697, 2010.

A Impedance and phase profiles for 2D and 3D linear systems: Analytic expressions

In order to analytically compute he impedance and phase profiles for 3D linear generic systems we use

$$\begin{cases} x' = a\,x + b\,y + c\,z + A_{in}\,e^{i\,\omega\,t}, \\ y' = \alpha\,x + p\,y \\ z' = \beta\,x + q\,z, \end{cases} \tag{44}$$

where a, b, c, α, β, p and q are constant, $\omega > 0$ and $A_{in} \geq 0$.

The characteristic polynomial for the corresponding homogeneous system ($A_{in} = 0$) is given by

$$r^3 - (a + p + q)\,r^2 + (a\,p + a\,q + p\,q - c\,\beta - b\,\alpha)\,r + b\,\alpha\,q + c\,\beta\,p - a\,p\,q = 0. \tag{45}$$

The particular solution to system (44) has the form

$$x_p(t) = A_{out}\, e^{i\,\omega\,t}, \qquad y_p(t) = B_{out}\, e^{i\,\omega\,t} \qquad \text{and} \qquad z_p(t) = C_{out}\, e^{i\,\omega\,t}, \tag{46}$$

Substituting (46) into system (44), rearranging terms, and solving the resulting algebraic system one obtains

$$Z(\omega) = \frac{A_{out}}{A_{in}} = \frac{P_r(\omega) + i\, P_i(\omega)}{Q_r(\omega) + i\, Q_i(\omega)} \tag{47}$$

where

$$P_r(\omega) = p\,q - \omega^2, \tag{48}$$

$$P_i(\omega) = -(p + q)\,\omega, \tag{49}$$

$$Q_r(\omega) = (a + p + q)\,\omega^2 - a\,p\,q + b\,\alpha\,q + c\,\beta\,p, \tag{50}$$

and

$$Q_i(\omega) = (a\,p + a\,q + p\,q - b\,\alpha - c\,\beta - \omega^2)\,\omega. \tag{51}$$

From (47)

$$|Z|^2(\omega) := \frac{A_{out}^2}{A_{in}^2} = \frac{P_r^2(\omega) + P_i^2(\omega)}{Q_r^2(\omega) + Q_i^2(\omega)} \tag{52}$$

and

$$\phi = \tan^{-1} \frac{P_r(\omega)\, Q_i(\omega) - P_i(\omega)\, Q_r(\omega)}{P_r(\omega)\, Q_r(\omega) + P_i(\omega)\, Q_i(\omega)}. \tag{53}$$

For a 2D linear system ($c = q = 0$), the characteristic polynomial for the corresponding homogeneous system ($A_{in} = 0$) is given by

$$r^2 - (a + p)\,r + (a\,p - b\,\alpha) = 0. \tag{54}$$

The roots of the characteristic polynomial are given by

$$r_{1,2} = \frac{(a + p) \pm \sqrt{(a - p)^2 + 4\,b\,\alpha}}{2}. \tag{55}$$

From eq. (55), the homogeneous (unforced) system displays oscillatory solutions with a natural frequency f_{nat} (Hz) given by

$$f_{nat} = \mu\, \frac{1000}{2\,\pi}, \qquad \mu = \sqrt{-4b\alpha - (a - p)^2}, \tag{56}$$

provided $4\,b\,\alpha + (a - p)^2 < 0$.

The impedance amplitude and phase are given, respectively, by

$$|Z(\omega)|^2 := \frac{A_{out}^2}{A_{in}^2} = \frac{p^2 + \omega^2}{[\,a\,p - b\,\alpha - \omega^2\,]^2 + (a + p)^2\,\omega^2}, \tag{57}$$

43

and

$$\phi(\omega) = \tan^{-1} \frac{(a\,p - b\,\alpha - \omega^2)\,\omega - (a+p)\,\omega\,p}{(a\,p - b\,\alpha - \omega^2)\,p + (a+p)\,\omega^2}. \tag{58}$$